
Collective Effects in the Hadron Future Circular Collider

Kollektive Effekte im Future Circular Collider für Hadronen
Zur Erlangung des Grades eines Doktors der Naturwissenschaften
(Dr. rer. nat.)
genehmigte Dissertation von Daria Astapovych aus Sumy/UdSSR
Tag der Einreichung: 28.01.2020, Tag der Prüfung: 28.04.2020
Darmstadt — D 17

1. Gutachten: Prof. Dr. rer. nat. Oliver Boine-Frankenheim
 2. Gutachten: Prof. Dr. rer. nat. habil. Ursula van Rienen
-



TECHNISCHE
UNIVERSITÄT
DARMSTADT

Fachbereich Elektrotechnik
und Informationstechnik
Institut für Teilchenbeschleunigung
und Elektromagnetische Felder

**Collective Effects in the Hadron Future Circular Collider
Kollektive Effekte im Future Circular Collider für Hadronen**

Genehmigte Dissertation von Daria Astapovych aus Sumy/UdSSR

- 1. Gutachten: Prof. Dr. rer. nat. Oliver Boine-Frankenheim**
- 2. Gutachten: Prof. Dr. rer. nat. habil. Ursula van Rienen**

Tag der Einreichung: 28.01.2020

Tag der Prüfung: 28.04.2020

Darmstadt – D 17

**Dieses Dokument wird bereitgestellt von tuprints,
E-Publishing-Service der TU Darmstadt**
<http://tuprints.ulb.tu-darmstadt.de>

Veröffentlicht unter der Lizenz: CC BY-SA 4.0 International
<https://creativecommons.org/licenses/by-sa/4.0/>

Erklärung zur Dissertation

Hiermit versichere ich, die vorliegende Dissertation ohne Hilfe Dritter und nur mit den angegebenen Quellen und Hilfsmitteln angefertigt zu haben. Alle Stellen, die aus Quellen entnommen wurden, sind als solche kenntlich gemacht. Diese Arbeit hat in gleicher oder ähnlicher Form noch keiner Prüfungsbehörde vorgelegen.

Darmstadt, den 28. Januar 2020

(Daria Astapovych)



Kurzfassung

Die Instabilität eines Strahls in Hadronen-Kreisbeschleunigern durch Koppelimpedanzen und Elektronenwolken wird untersucht. Der Future Circular Collider für Hadronen-Hadronen-Stöße (FCC-hh) ist ein möglicher Nachfolger des Large Hadron Collider (LHC). Der FCC-hh soll mit einer Kollisionsenergie von 100 TeV in einem Tunnel mit einem Umfang von 100 km betrieben werden, im Vergleich zu 14 TeV-Kollisionsenergie und 27 km Umfang für den LHC. Ähnlich wie beim LHC kann auch beim FCC-hh die innere Vakuumkammer ein limitierender Faktor für die Strahlstabilität sein. Die elektromagnetische Wechselwirkung von Strahl und Kammer wird durch eine Strahlkoppelimpedanz beschrieben, während die Wechselwirkung zwischen dem Strahl und den freien Elektronen im Strahlrohr zur Bildung der Elektronenwolke führt. Die Leistungsfähigkeit des Colliders kann durch Strahlinstabilitäten, Strahlverluste, Wärmebelastung und Vakuumdegradation beeinträchtigt werden.

Absolute Vorhersagen von kollektiven Effekten erfordern eine möglichst realistische Beschreibung der Gesamtimpedanz. Aufgrund der Unsicherheiten in den elektromagnetischen Materialeigenschaften und fehlender Komponentendetails in der gegenwärtigen Entwurfsphase der Kammer würden die absoluten Schätzungen große Fehlerbalken aufweisen. Stattdessen konzentriert sich diese Arbeit auf die Skalierung der kollektiven Effekte mit der Strahlenergie und der Kammergeometrie vom LHC bis zum FCC-hh, da dies tatsächliche Beobachtungen an einem bestehenden Collider zu einem neuen mit vielen Ähnlichkeiten in Beziehung setzen kann.

Die Impedanzen werden für die detaillierten transversalen Querschnitte für die FCC-hh und die LHC Kammern berechnet. Es hat sich gezeigt, dass das aktuelle Design der FCC-hh Kammer einen wesentlichen Beitrag zur Gesamtimpedanz leistet. Basierend auf einer Analyse der durch die Impedanz bedingten Effekte schlägt diese Arbeit Änderungen im Design der Kammer vor, um dessen Impedanzbeitrag zu reduzieren.

Eine Studie zur Entstehung von Elektronenwolken wird ebenfalls für die detaillierten Querschnitte für die FCC-hh und die LHC Kammern durchgeführt. Als ein Ergebnis dieser Studien kann geschlossen werden, dass eine zusätzli-

che Beschichtung der inneren FCC-hh Kammer erforderlich ist, um die durch die Elektronenwolke verursachten Effekte abzuschwächen. Zur Untersuchung der Auswirkungen auf die durch die Elektronenwolke hervorgerufenen Effekte aufgrund der höheren Strahlenergie und der kleineren Apertur des FCC-hh-Strahlenschirms im Vergleich zum LHC wird außerdem eine Untersuchung des Wärmeeintrags durchgeführt.


Abstract

The instability of a beam in hadron circular accelerators due to the beam coupling impedance and electron clouds is investigated. The Future hadron-hadron Circular Collider (FCC-hh) is a potential successor of the Large Hadron Collider (LHC). FCC-hh will operate at 100 TeV collision energy in a tunnel with a circumference of 100 km, in comparison to 14 TeV collision energy and 27 km circumference in the LHC. Similarly to the LHC, in the FCC-hh the beam screen can be a limiting factor for beam stability. The electromagnetic interaction of the beam and beam screen is described by a beam coupling impedance, whereas the interaction between the beam and free electrons in the beam pipe leads to the formation of the electron cloud. As a result, machine performance can be affected by beam instabilities, beam losses, heat load, and vacuum degradation.

Absolute predictions of collective effects require the most realistic impedance database. Because of uncertainties in the electromagnetic material properties and missing component details at the present design stage of the beam screen, the absolute estimations would carry large error bars. Instead, this thesis focuses on the scaling of collective effects with beam energy and beam screen geometry from LHC to FCC-hh, as this can relate actual observations from an existing collider to a new one, with many similarities.

The impedances are computed for the detailed transverse cross-section for the FCC-hh and the LHC beam screens. The current design of the FCC-hh beam screen is found to make a significant contribution to impedance. Based on an analysis of impedance-induced effects, this thesis work proposes modifications in the beam screen design to mitigate its impedance contribution.

An electron cloud buildup study is also performed for the detailed transverse cross-section for the FCC-hh and the LHC beam screens. As a result of these computations, one can conclude that an additional coating on the FCC-hh beam screen is required to mitigate the effects driven by the electron cloud. Further, to investigate the impact on the effects induced by electron clouds due to the higher beam energy and smaller aperture of FCC-hh beam screen in



comparison to LHC, a study of the heat load with beam energy and pipe radius is performed.

Contents

1. Introduction	1
2. Single Particle Dynamics	7
2.1. Transverse Particle Dynamics	8
2.2. Longitudinal Particle Dynamics	10
3. Impedance and Collective Effects	13
3.1. Basic Impedance Theory	13
3.2. Impedance-Induced Effects	17
3.2.1. Bunch Modes	18
3.2.2. Effective Impedance	19
3.2.3. Collective Effects	21
3.2.4. Heat Load	24
3.3. Techniques of Impedance-Induced Effects Mitigation	25
4. Electron Cloud Effects	27
4.1. Secondary Electron Emission	27
4.2. Electron Cloud Buildup	30
4.3. Secondary Electron Emission Yield Model	31
4.4. Electron-Cloud-Induced Effects	35
4.4.1. Energy Gain in Electron Cloud	36
4.4.2. Electron-Cloud-Induced Heat Load	38
4.5. Techniques of Electron Cloud Mitigation	39
5. Simulation Tools and Methods	41
5.1. BeamImpedance2D	41
5.2. openECLoud	42
5.3. pySimEC	43
5.4. Electron Cloud Map Formalism	44
6. Beam Screen Impedance and Impedance-Induced Effects in FCC-hh	49
6.1. Beam Screen Impedance	49



6.2. Collective Effects	53
6.2.1. Transverse Coupled-Bunch Instability	54
6.2.2. Transverse Mode Coupling Instability	55
6.2.3. Heat Load	56
6.3. Effects of the Beam Screen Coating	58
6.3.1. Amorphous Carbon Coating	58
6.3.2. Copper Coating Thickness	60
6.3.3. Copper Coating Resistivity	61
7. Electron Cloud Effects in FCC-hh	65
7.1. Secondary Electron Yield Threshold	65
7.1.1. Electron Cloud Buildup	65
7.1.2. Secondary Electron Yield Threshold for FCC-hh and LHC	68
7.1.3. Secondary Emission Yield Threshold for Circular Beam Pipe	69
7.1.4. Energy Gain in Electron Cloud	72
7.2. Electron Cloud Map	73
7.3. Heat Load due to Electron Cloud	77
7.3.1. Heat Load Scaling with Beam Pipe Radius	78
7.3.2. Heat Load Scaling with Beam Radius	79
7.3.3. Analytic Approach to Stopping Power	82
8. Conclusions	85
Appendix A. Secondary Electron Emission Yield Models	89
Bibliography	109

1 Introduction

In July 2012, the two experiments ATLAS and CMS at LHC reported evidence for the Higgs boson particle with a rest mass energy around $125 \text{ GeV}/c^2$. However, fundamental questions concerning a dark matter, matter-antimatter asymmetry, and the neutrino mass remain open. There is also a possibility of physics beyond the Standard Model [1, 2]. A hadron-hadron collider, particularly a proton-proton collider can resolve these fundamental questions by achieving a sufficient increase in energy limit. Further, a lepton-hadron collider particularly an electron-proton collider can also achieve high-precision measurements of Higgs boson properties and to search for the rare decays predicted by the physics beyond the Standard Model.

One of the main characteristics of a particle collider is the luminosity, which is defined by the number of events generated during the collisions in a collider [3]. The planned upgrade of the LHC to achieve a high-luminosity will increase the collision rate in the experiments by a factor 10 [4]. Besides this, the European Strategy Group for Particle Physics initiated the Future Circular Collider (FCC) study of the post-LHC era accelerators in 2014 [5, 6]. The three main proposed projects in this study are: high-energy LHC (HE-LHC), e^+e^- (FCC-ee) and pp (FCC-hh) colliders. The additional option is to include pe^- (FCC-he) collider with the aim of the proton quarks structure study. All options have their own goals. Thus, HE-LHC is planned to obtain more statistics. Then, the FCC-ee continues with highly precise measurements of the Standard Model. Finally, the FCC-hh together with the FCC-he will work on the particular questions and searches for the new physics. The main parameters and the characteristics of these colliders are briefly summarised in the conceptual design report [7]. The main focus of this thesis is the collective effects in the FCC-hh, whose main parameters are described in this chapter.

Future Circular Hadron Collider

The FCC-hh is a proton-proton collider with 100 TeV of centre-of-mass energy with an option for heavy-ion operation. The circumference of the machine is supposed to be 100 km, which is defined by the magnetic field strength of the

16 T Nb3Sn dipole magnets. Since the FCC-hh is the next step of LHC, therefore the LHC is a possible consideration of a beam injector for it. In comparison to the LHC, the beam energy in the FCC-hh is seven times higher and the luminosity is 30 times higher. Table 1.1 presents the baseline beam and machine parameters for the FCC-hh and the LHC. The physics of FCC-hh case is based on following goals [7–9]:

- to measure the top quark-Higgs interaction and to obtain the statistics for improving the separation of the Higgs boson signal from the background,
- to observe the new particle at the reachable higher energy,
- to answer the questions about dark matter origin, electroweak phase transition.

Also, the essential advantage of the FCC-hh over the FCC-ee experiments is the possible observation of self-coupling of the Higgs boson due to the larger statistics.

Parameters, symbol [unit]	FCC-hh	LHC
Circumference, C [km]	97.75	26.7
Dipole field, B [T]	16	8.33
Injection beam energy, E_{inj} [TeV]	3.3	0.45
Flat-top beam energy, E_{top} [TeV]	50	6.5
Peak luminosity, L [$\text{cm}^{-2}\text{s}^{-1}$]	30×10^{34}	1.0×10^{34}
Bunch intensity, N_b [ppb]	10^{11}	1.15×10^{11}
Number of bunches, M	10400	2808
Bunch spacing, t_s [ns]	25	25
Bunch length, σ_τ at E_{inj} [ns]	1.07	1.5
Bunch length, σ_τ at E_{top} [ns]	1.07	1.08
Normalized emittance, ε_n at E_{top} [μm]	2.2	2.5
Betatron tune, Q_x/Q_y at E_{inj}	111.28/109.31	59.28/63.31
Betatron tune, Q_x/Q_y at E_{top}	111.31/109.32	59.31/63.32
Synchrotron tune, Q_s at E_{inj}	2.8×10^{-3}	5.1×10^{-3}
Synchrotron tune, Q_s at E_{top}	1.2×10^{-3}	2.2×10^{-3}

Table 1.1.: FCC-hh and LHC key parameters. Note that here “flat-top” and “top” energy is the top energy without collision.

Beam Screen Design

The achievable luminosity in a particle accelerator is usually limited by the characteristics of beam surroundings. Considering the experience at LHC, one of the critical elements of accelerator to control the beam quality is the beam screen. Thus, small aperture together with the complex opening slits in the FCC-hh beam screen might be a limiting factor for the beam stability and quality.

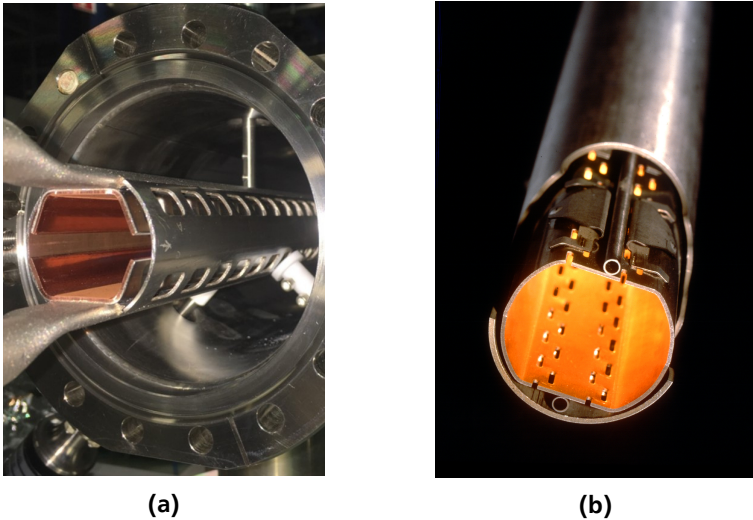


Figure 1.1.: (a) FCC-hh [10] and (b) LHC [11] beam screen photos.

Figure 1.1(a) shows the beam screens of the current FCC-hh prototype (courtesy by L. A. Gonzalez). Figure 1.1(b) shows the LHC beam screen. The high total power of the synchrotron radiation of about ≈ 2.3 MW in the cold arcs [12] is one of the main reasons to design the complex and sophisticated beam screen for the FCC-hh in comparison with the simple one in the LHC. As seen in Fig. 1.1(a) two slits in the primary chamber are used to deflect the photons, which are generated due to the high beam energy. The synchrotron radiation will be absorbed when photons reflect from the saw-teeth on the secondary chamber also seen in Fig. 1.1(a).

The current FCC-hh design, which is similar to LHC assumes a tube with stainless steel to resist the mechanical stresses, and a copper-coating layer to minimise the resistive wall losses. Additionally, the saw-tooth pattern on the secondary chamber will be imprinted on copper. Furthermore, the amorphous carbon (a-C) coating is considered to prevent the electron cloud buildup.

Motivation

The electromagnetic interaction between a beam and a beam pipe is described by a beam coupling impedance. Impedance depends on geometry and material of the beam pipe. As a results, this interaction can lead to the impedance-induced effects, or collective effects. Furthermore, the free electrons in the beam pipe produced by residual gas ionisation or photoemission due to the synchrotron radiation can be accelerated by the beam electromagnetic field towards the pipe walls. Depending on the impact energy of these electrons and the properties of the surface, the secondary electrons can be generated. The short relativistic proton bunches and small spacing between them can lead to an avalanche process of electron multiplication with the formation of the so-called electron cloud. The uncontrollable electron cloud is a significant issue causing beam quality degradation, beam instabilities, as well as vacuum degradation. The aim of this thesis is to analyse the FCC-hh beam stability in terms of the beam screen impedance and the electron clouds. The results are also compared to the LHC.

A two-dimensional finite element solver BeamImpedance2D is used to compute the impedances for the detailed transverse cross-section of the FCC-hh and the LHC beam screens. The results of impedance-induced effects particularly transverse coupled-bunch instability growth rate, transverse mode-coupling instability threshold and heat load are analysed for FCC-hh and compared with LHC.

The electron cloud buildup simulations are performed with the openELOUD tool together with the detailed transverse cross-section of the FCC-hh and the LHC beam screens. Based on these results, the need for amorphous carbon coating is revealed to reduce the secondary electron yield on the material surface. Since a new layer on the beam screen can affect its impedance, a numerical study on the optimal thickness of amorphous carbon coating is performed. Comparing FCC-hh and LHC, one can see that FCC-hh has twice smaller beam screen aperture and the flat-top (top energy without collision) beam energy is one order of magnitude higher. To reveal the impact of these parameters

on the effects induced by electron clouds, a study of the heat load with beam energy and pipe radius is conducted. Therefore, a semi-analytic tracking code pySimEC, which allows simulating the electron cloud buildup in the circular beam pipe is developed.

It is worth noting that due to the uncertainties in the material properties and missing component details, the absolute estimations will include large error-bars. Therefore, the scaling of effects induced by beam screen impedance and electron cloud with beam energy and beam screen geometry from LHC to FCC-hh is investigated in this thesis.

Overview of the Thesis

This thesis is organised as follows: the introduction to the basic concepts of accelerator physics, such as particle motion in the synchrotron in transverse and longitudinal planes is explained in Chapter 2. The electromagnetic interaction between the beam and its surrounding is described in Chapter 3. This chapter also covers the resulting effects of this interaction such as beam instabilities and heat load. Chapter 4 presents the concept of the electron cloud in accelerator together with the effects due to the interaction between electron cloud and beam. The simulation tools and methods used in this thesis are described in Chapter 5. The results of the study on the impedance and impedance-induced effects on the beam dynamics are discussed in Chapter 6. The impact of the amorphous carbon coating in the beam screen and the impact of the copper properties is also analysed. Chapter 7 presents the results of the electron cloud effects study. Finally, the results of this thesis are briefly concluded in Chapter 8.



2 Single Particle Dynamics

The motion of a single particle of charge q , mass m , and velocity \vec{v} in the electromagnetic field is described by the Lorentz force \vec{F} [13]

$$\vec{F} = \frac{d\vec{p}}{dt} = q(\vec{E} + \vec{v} \times \vec{B}), \quad (2.1)$$

where $\vec{p} = \gamma m \vec{v}$ is the particle momentum, $\gamma = 1/\sqrt{1 - \beta^2}$ is the relativistic factor with the relativistic velocity $\beta = v/c$ and c is the speed of light. \vec{E} is the electric field strength and \vec{B} is the magnetic flux density. Here, \vec{E} and \vec{B} are defined in terms of the scalar potential ϕ and the vector potential \vec{A}

$$\vec{E} = -\nabla\phi - \frac{\partial\vec{A}}{\partial t}, \quad \vec{B} = \nabla \times \vec{A}. \quad (2.2)$$

In a particle accelerator, the electric field accelerates particles, while the magnetic field steers their trajectories. If the magnetic field is homogeneous and perpendicular to the velocity of the particle, the particle has a circular trajectory with the bending radius ρ , leading to the relation

$$B\rho = \frac{p}{q}. \quad (2.3)$$

$B\rho$ is known as the magnetic rigidity. It is a measure of the particle momentum while passing through a magnetic field. It can be seen from Eq. 2.3 that a particle with a smaller momentum will have a smaller resistance to the magnetic field deflection [14].

Coordinate System

To describe the particle motion in a synchrotron one can introduce a co-moving coordinate system as shown in Fig. 2.1. A particle which travels along the reference orbit is known as a reference particle.

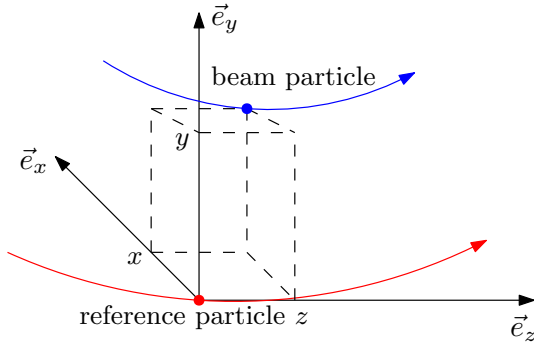


Figure 2.1.: The co-moving coordinate system in an accelerator.

The position of the reference particle with the velocity v_0 and momentum p_0 at time t is defined as $s = \int_0^t v_0 d\tau$. This is an independent parameter along the particle trajectory. The coordinates of a beam particle in a co-moving coordinate system are given by a vector $(x, x', y, y', z, \Delta p/p_0)$, where x, y are the particle transverse coordinates and z is the particle longitudinal coordinate, $x' = dx/ds$ and $y' = dy/ds$ denote the transverse angular deflections which are the derivatives of x and y with respect to distance s along the particle trajectory, respectively. Here, $\Delta p/p_0 = (p - p_0)/p_0$ is the momentum spread with respect to reference momentum.

The convention in this thesis considers that a particle which is ahead of the reference particle has $z > 0$ and a particle which is behind the reference particle has $z < 0$.

A detailed introduction to the single particle and beam dynamics can be found in Refs. [15–17].

2.1 Transverse Particle Dynamics

A synchrotron is a particular case of a circular accelerator, so the particle motion is periodic in it. Consider a charged particle with $\Delta p/p_0 = 0$ and $z = 0$, which moves in a synchrotron with circumference C . The linearised equation of motion in the transverse plane can be written as [14, 18]

$$u''(s) + K_u(s)u(s) = 0, \quad (2.4)$$

where $u(s)$ stands for $x(s)$ or $y(s)$. $K(s)$ is a periodic focusing function, which leads to relation $K(s) = K(s + C)$. Eq. 2.4 is known as Hill's equation of motion, which describes the transverse oscillations of the particle. The solution of this equation in terms of phase-amplitude variables is written as

$$u(s) = \sqrt{\varepsilon_u \beta_u(s)} \cos(\psi_u(s) + \varphi_0),$$

$$u'(s) = -\sqrt{\frac{\varepsilon_u}{\beta_u(s)}} [\alpha_u \cos(\psi_u(s) + \varphi_0) - \sin(\psi_u(s) + \varphi_0)],$$
(2.5)

where β_u , $\alpha_u = -\beta'_u/2$, $\gamma_u = (1 + \alpha_u^2)/\beta_u$ are the Twiss parameters. ε_u is the single-particle emittance, which is discussed below. The function β_u defines the amplitude of the particle oscillations known as betatron oscillations. Consider the root mean square (rms) particle size σ_u one can write a relation $\sigma_u = \sqrt{\varepsilon_u \beta_u}$. φ_0 is the initial phase and the betatron phase ψ_u is defined as

$$\psi_u = \int_0^s \frac{ds}{\beta_u(s)}.$$
(2.6)

Figure 2.2 shows the single-particle phase space ellipse. The enclosed area is known as particle emittance and is defined as

$$\varepsilon_u = \gamma_u(s)u^2(s) + 2\alpha_u(s)u(s)u'(s) + \beta_u(s)u'^2(s),$$
(2.7)

It is convenient to define the emittance that is preserved with acceleration and known as the normalised emittance $\varepsilon_{n,u} = \beta\gamma\varepsilon_u$.

The number of betatron oscillations per one revolution is known as *betatron tune*

$$Q_u = \frac{1}{2\pi} \Delta\psi_u = \frac{1}{2\pi} \oint \frac{ds}{\beta_u(s)}.$$
(2.8)

The ratio of the tune spread to the momentum spread is known as the *chromaticity*

$$\xi_u = \frac{dQ_u}{Q_u} \bigg/ \frac{dp}{p_0}.$$
(2.9)

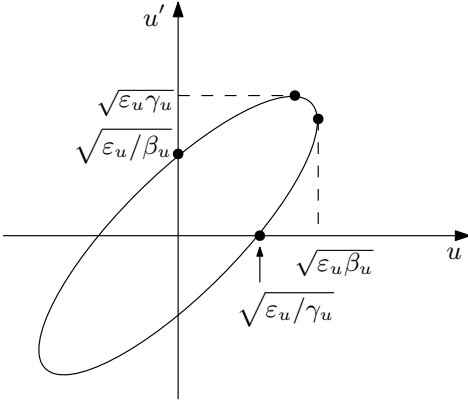


Figure 2.2.: The single-particle phase space ellipse with the area of $\pi\varepsilon$. α_u and β_u are related to the particle slope and shape, respectively, while γ_u is dependent on α_u and β_u .

2.2 Longitudinal Particle Dynamics

In the longitudinal phase space ($z, \Delta p/p$) the beam can be either coasting or bunched. In the coasting beams, charged particles are smoothly distributed along the synchrotron and move with the constant longitudinal velocity. In the case of bunched beams, charged particles are gathered longitudinally by an radio-frequency (RF) field.

The reference particle with angular revolution frequency $\omega_0 = 2\pi\beta c/C$, and which is synchronised with the RF phase ϕ_0 , is called a *synchronous particle*. At the same time, the off-momentum particle, which has the orbit different from the reference particle due to dispersion, performs the *synchrotron oscillations* in the longitudinal plane. Assuming the sinusoidal electric field of the RF cavity, the equations of synchrotron motion for these particles can be written as [14]

$$\frac{d\Delta p}{dt} = \frac{\omega_0 q V}{2\pi\gamma m\beta^2 c^2} (\sin\phi - \sin\phi_0), \quad (2.10)$$

$$\frac{d\phi}{dt} = \omega_0 h \eta \frac{\Delta p}{p_0}, \quad (2.11)$$

where V is the RF voltage, $\phi = \phi_0 + 2\pi h z/C$ is the phase for the off-momentum particle with the phase of the reference particle ϕ_0 , and h is the harmonic number of the RF system, which defines the maximum number of bunches

that can be loaded into the accelerator. The slip factor η defines the change in the revolution period with respect to the particle energy [14].

Substituting $\Delta p/p_0$ from Eq. 2.10 to differentiated Eq. 2.11, one can obtain the equation of motion for the phase

$$\frac{d^2(\phi - \phi_0)}{dt^2} = \frac{\omega_0^2 h \eta q V}{2\pi m \gamma \beta^2 c^2} (\sin \phi - \sin \phi_0) \approx -\Omega_s^2 (\phi - \phi_0), \quad (2.12)$$

where Ω_s is the angular synchrotron frequency:

$$\Omega_s = \omega_0 \sqrt{\frac{qhV|\eta \cos \phi_0|}{2\pi m \gamma \beta^2 c^2}}. \quad (2.13)$$

Similar to the betatron motion characteristics, the number of synchrotron oscillations per revolution period is known as *synchrotron tune*

$$Q_s = \frac{\Omega_s}{\omega_0}. \quad (2.14)$$



3 Impedance and Collective Effects

This chapter covers the basic theory on the resistive wall impedance together with induced effects on the beam of charged particles. Section 3.1 presents the fundamentals of impedance theory. Section 3.2 includes the impedance-induced effects as transverse coupled-bunch instability and transverse mode coupling instability, and heat load. Section 3.3 deals with possible mitigation techniques for collective effects induced by the impedance.

3.1 Basic Impedance Theory

Consider a beam of two charged particles q_1 and q_2 with constant velocity $v \approx c$ travelling through a vacuum chamber along the symmetry axis z . The particle q_2 moves at a distance s behind the particle q_1 as shown in Fig. 3.1a. If the vacuum chamber is perfectly conducting and smooth, the particle q_2 is not affected by any forces. However, if the vacuum chamber is not perfectly conducting or has any changes in structure as shown in Fig. 3.1 (b), the first particle interacts with it and creates an electromagnetic field known as a wake field [16, 19]. This field can affect the second particle and perturb its motion.

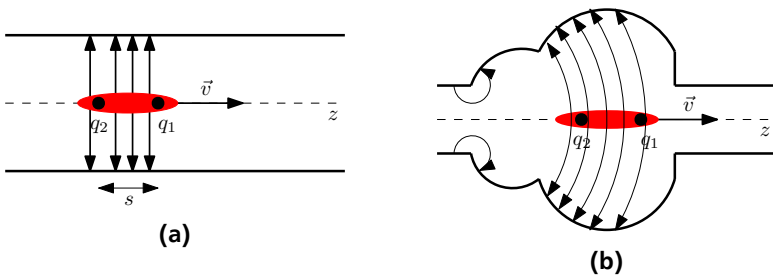


Figure 3.1.: Example of the wake field generated by the beam in the vacuum beam chamber that (a) is smooth and not perfectly conducting and (b) has changes in structure.

The interaction between the wake field and the beam with an arbitrary density distribution is determined by the wake potential V

$$V(s) = q \int_0^{\infty} W(z) \lambda(s-z) dz, \quad (3.1)$$

where the wake potential is a convolution of the wake function W with the normalised beam linear density λ . The wake potential, and the wake function has longitudinal and horizontal components. The longitudinal wake potential is a voltage gain of a unit charge due to the wake field. The transverse wake potential is the transverse momentum kick that the beam undergoes due to the deflecting fields [20]. As the magnetic field is perpendicular to the particle trajectory and does not affect the longitudinal motion, the longitudinal wake function is obtained by integrating the E_z component of the electric field

$$W_{\parallel}(s) = -\frac{1}{q} \int_{-\infty}^{\infty} E_z dz. \quad (3.2)$$

The transverse wake function is defined as an integral of transverse electromagnetic force normalised by the transverse displacement r of the charged particle

$$\vec{W}_{\perp}(s) = -\frac{1}{qr} \int_{-\infty}^{\infty} (\vec{E} + \vec{v} \times \vec{B})_{\perp} dz. \quad (3.3)$$

Whereas the longitudinal wake function is a scalar, transverse wake function is a vector and has horizontal and vertical components. It is important to note that the wake function is determined only by the shape and electromagnetic properties of the structure and does not depend on the beam distribution [16]. The relation between the longitudinal W_{\parallel} and transverse W_{\perp} wake functions is given by the Panofsky-Wenzel theorem [16]

$$\nabla W_{\parallel} = \frac{\partial \vec{W}_{\perp}}{\partial s}. \quad (3.4)$$

In a circular accelerator, the frequency domain is convenient to compute the wake fields as compared to time domain because the beam passes periodically the same position of the machine [20]. Applying the frequency Fourier trans-

formation to Eqs. 3.2 and 3.3, one can obtain the longitudinal and transverse beam coupling impedances as follows:

$$\begin{aligned} Z_{\parallel}(\omega) &= \int_{-\infty}^{\infty} W_{\parallel}(s) e^{-i\omega s/c} \frac{ds}{c}, \\ Z_{\perp}(\omega) &= i \int_{-\infty}^{\infty} W_{\perp}(s) e^{-i\omega s/c} \frac{ds}{c}. \end{aligned} \quad (3.5)$$

Similarly to the transverse wake functions the transverse impedance has longitudinal and horizontal components.

The exact transverse and longitudinal resistive wall impedance for a cylindrical pipe with the length L , radius b and a material of resistivity ρ can be written as [16]

$$Z_{\perp}(\omega) = (1 - i \operatorname{sgn}(\omega)) \frac{cL\rho}{\omega\pi b^3 \delta_{\text{skin}}}, \quad (3.6)$$

$$Z_{\parallel}(\omega) = (1 - i \operatorname{sgn}(\omega)) \frac{L\rho}{2\pi b \delta_{\text{skin}}}, \quad (3.7)$$

where the skin depth

$$\delta_{\text{skin}} = \sqrt{\frac{2c\rho}{Z_0\mu_r\omega}} = \sqrt{\frac{2\rho}{\mu_r\mu_0\omega}}, \quad (3.8)$$

where $Z_0 = \sqrt{\mu_0/\varepsilon_0} = 377 \Omega$ is the impedance of free space with the magnetic permeability μ_0 and the electric permittivity ε_0 of free space. μ_r is the relative magnetic beam pipe permeability. These formulas are known as a thick-wall impedance approximation, which is based on the skin depth effect. However, the skin depth is larger than the thickness d of the wall at low frequency. Thus, a thin-wall approximation for the impedance can be used [21, 22]

$$Z_{\perp}(\omega) = (1 - i) \frac{cL\rho}{\omega\pi b^3 d}, \quad (3.9)$$

$$Z_{\parallel}(\omega) = (1 - i) \frac{L\rho}{2\pi b d}. \quad (3.10)$$

It can be seen from Eqs. 3.6 – 3.10 that the impedance depends on the material resistivity, the thickness of the material, and the beam pipe radius.

Based on the effective wake field range, there are two types of coupling impedance: broadband and narrowband. The broadband impedance corresponds to the short-range wake field resulting in the single bunch dynamics, for example, vacuum chamber gaps, breaks, joints, bellows, tapers, beam position monitors. The narrowband impedance corresponds to the long-range wake field leading to the multibunch dynamics effects, for example, of this impedance are RF cavity, resistive wall.

The coupling impedance due to the finite resistivity of the beam vacuum chamber is known as the resistive wall impedance.

Electrical Resistivity

The resistivity of the beam pipe wall is a principal source of the impedance. It can be seen from Eq. 3.6 that to have a sufficiently low impedance, it is important to choose a material with a rather low resistivity. The resistivity of the normal conductors, such as copper used in the FCC-hh beam screen (Chapter 1), does not depend much on the purity of the material at room temperature. Nevertheless, at low temperature it is strongly affected by the impurity content and the external magnetic field B .

For the temperature range of $\pm 200^\circ\text{C}$ the resistivity has a linear dependence on temperature [23]

$$\rho(T) = \rho_0(1 + \alpha(T - T_0)), \quad (3.11)$$

where α is the temperature coefficient, T_0 is the reference temperature, and ρ_0 is the resistivity at temperature T_0 . However, at the temperature lower than -200° degrees, which is a case of the FCC-hh, the resistivity does not follow this rule and the values can be found in Refs. [24–27].

The electrical resistivity at low temperature is useful for determining the chemical purity and mechanical state of the material [24]. For indication of material properties such as hardening and purity a so-called residual-resistance ratio (RRR) is used [28]:

$$\text{RRR} = \rho(300\text{ K})/\rho(4\text{ K}).$$

The dependence of the resistivity on the external magnetic field is called magnetoresistance. The magnetoresistance effect for the pure metals usually follows the Kohler's rule [29]

$$\Delta\rho/\rho = f(B/\rho(T)). \quad (3.12)$$

The magnetoresistivity for copper is defined as [30]

$$\rho(T, B) = \rho(T, 0) \times [1 + 10^{-2.69}(B \times RRR_0)^{1.055}], \quad (3.13)$$

where $RRR_0 = \rho(273 \text{ K})/\rho(T)$ is RRR at temperature T , and resistivity $\rho_{\text{Cu}}(273 \text{ K}) = 1.5 \times 10^{-8} \Omega\text{m}$.

Table 3.1 shows the resistivity values of copper (Cu) and stainless steel used in the FCC-hh and the LHC beam screens. The values for copper are obtained using Eq. 3.13. It is worth mentioning that during the conceptual design of the LHC, the copper in the beam screen was assumed with $RRR = 100$, but due to the selected manufacturing process this value was lowered to 70 [31, 32]. Here the copper resistivity for the FCC-hh and LHC are based on a $RRR = 70$.

Material name	T [K]	$\rho(B_0)$ [Ωm]	$\rho(B_{\text{inj}})$ [Ωm]	$\rho(B_{\text{top}})$ [Ωm]
$\text{Cu}_{\text{FCC-hh}}$	50	7.5×10^{-10}	7.88×10^{-10}	1.42×10^{-9}
Cu_{LHC}	20	2.4×10^{-10}	2.8×10^{-10}	7.7×10^{-10}
Stainless steel	20/50	6×10^{-7}		

Table 3.1.: Resistivities for the LHC and the FCC-hh beam screen coatings. B_0 is for the case of the absence of a magnetic field. B_{inj} and B_{top} are 1.06 and 16 T for the FCC-hh and 0.54 and 8.3 T for the LHC.

The stainless steel used in the LHC beam screen is non-magnetic, that is the magnetic field does not affect its electrical resistivity. Additionally, the chosen grade has a low magnetic permeability and can be used at cryogenic temperatures without any changes in the resistivity [33]. Thus, the resistivity of the stainless steel is the same for both FCC-hh and LHC.

3.2 Impedance-Induced Effects

The interaction between the beam and the resistive wall can lead to the collective effects, which can be divided into two groups [34]:

-
1. Incoherent effects: it occurs due to the interaction between a single particle and the electromagnetic field produced by all other particles.
 2. Coherent effects: it occurs due to the interaction between the whole beam and its surroundings.

Section 3.2.1 describes the motion of the bunches in a synchrotron. The interaction between the coupling impedance and the beam can be described by the effective impedance described in Section 3.2.2. Examples of multibunch effect and single-bunch effect are given in Sec. 3.2.3. Section 3.2.4 covers such coherent effect as the heat load, or energy loss which related to the impact of the longitudinal impedance. More examples of the collective effects can be found in [15, 16, 34].

3.2.1 Bunch Modes

The motion of the bunched beam in both planes can be characterised by the mode numbers. Thus, in the transverse plane, the motion is usually described by two mode numbers [35]:

- coupled-bunch mode number n , defined as the number of waves of coherent bunch motion along the synchrotron and is related to the bunch-to-bunch phase shift as $\Delta\phi = 2\pi n/M$, where M is the number of bunches in the beam. Figure 3.2 shows an example of the modes $n = 0, 1, 2$ in the case of four bunches;
- within-bunch mode number m , also known as the head-tail mode number. It is defined as the number of the betatron wavelengths per synchrotron period at a given moment. Figure 3.3 shows an example of the modes $m = 0, 1, 2$ in the case of the single bunch.

As for the longitudinal plane, the motion is also described by the similar two mode numbers:

- coupled-bunch mode number n , defined as the number of coherent motion waves per revolution, and related to the bunch-to-bunch phase shift as $\Delta\phi = 2\pi n/M$, where M is the number of bunches in the beam;
- within-bunch mode number m , defined as a number of density modulation periods per synchrotron period.

The concept of mode numbers is used to study the bunch instabilities, which may occur as a result of the interaction between the bunch and its surroundings. The transverse mode number n is used to analyse the transverse coupled-

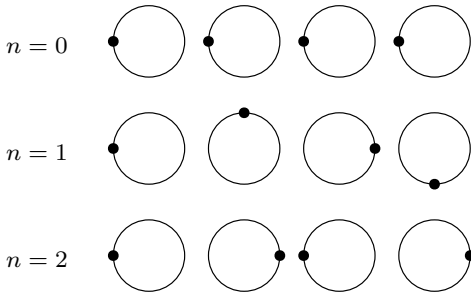


Figure 3.2.: Example of transverse coupled-bunch modes n for four bunches in the synchrotron.

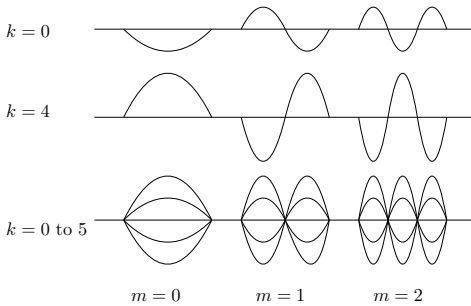


Figure 3.3.: Example of head-tail modes m for a single bunch in the synchrotron.

bunch instability, while the transverse mode number m is used in analysis of the transverse mode coupling instability (Sec. 3.2.3).

3.2.2 Effective Impedance

The interaction between the coasting beam and its surrounding can be described by the coupling impedance. If the beam consists of bunches, the impedance is defined at an infinite number of discrete frequencies, which is given by the mode spectrum [36]. Then, the transverse effective impedance can be written as

$$Z_{\perp}^{\text{eff}} = \frac{\sum \beta_{\perp} Z_{\perp}(\omega) h_{nm}(\omega - \omega_{\xi})}{\beta_{\perp} \sum_p h_{nm}(\omega - \omega_{\xi})}, \quad (3.14)$$

where the summation is performed over the transverse impedance Z_{\perp} and the bunch power spectrum $h_{nm}(\omega)$ of the n -th azimuthal and m -th radial modes. β_{\perp} is a local β -function, and $\tilde{\beta}_{\perp} = C/(2\pi Q_{x,y})$. $\omega_{\xi} = (\xi\omega_0/\eta)$ is the chromatic angular frequency, where ξ is the chromaticity and η is a slip factor. Similar formula can be written for the longitudinal effective impedance.

The power spectrum of the bunch with rms length σ and linear distribution is defined as

$$h(\omega, \sigma) = \tilde{\lambda}(\omega) \tilde{\lambda}^*(\omega), \quad (3.15)$$

where $\tilde{\lambda}(\omega)$ is a Fourier transform of the linear distribution $\lambda(\tau)$ and is defined as [15]

$$\tilde{\lambda}(\omega) = \int_{-\infty}^{\infty} \lambda(\tau) e^{-i\omega\tau} d\tau. \quad (3.16)$$

For a bunch with the radial mode number $m = 0$ and a Gaussian distribution, the line density and the power density are defined as following [19]

$$\lambda(\tau) = \frac{1}{\sqrt{2\pi}\sigma_{\tau}} \exp\left(-\frac{\tau^2}{2\sigma_{\tau}^2}\right), \quad (3.17)$$

$$h_n(\omega) = (\omega\sigma_{\tau})^{2n} \exp(-\omega^2\sigma_{\tau}^2),$$

where $\sigma_{\tau} = \beta c \sigma_z$ is rms bunch length in [s] with the bunch length σ_z in [m].

Since the head-tail excitations are sinusoidal-like, the line density can be approximated by sinusoidal functions. This approximation was done by F. Sacherer [37] and these head-tail modes are called Sacherer's sinusoidal modes. For the case of azimuthal bunch modes n and the most excited radial

mode $m = 0$, the line density $\lambda(\tau)$ and the power density $h(\omega)$ are defined as [15]

$$\lambda_n(\tau) \propto \begin{cases} \cos \frac{(n+1)\pi\tau}{\sigma_\tau} & n = 0, 2, \dots, \\ \sin \frac{(n+1)\pi\tau}{\sigma_\tau} & n = 1, 3, \dots, \end{cases} \quad (3.18)$$

$$h_n(\omega) = \frac{4(n+1)^2}{\pi^2} \frac{1 + (-1)^n \cos(\pi y)}{[y^2 - (n+1)^2]^2}, \quad y = \omega\sigma_\tau/\pi.$$

In the case of a single bunch the summation in Eq. 3.14 is done over the mode spectrum lines at frequencies

$$\omega_p = (p + Q_{x,y})\omega_0, \quad -\infty < p < \infty. \quad (3.19)$$

In the case of a beam with M equally spaced bunches and coupled-bunch mode n , the summation is done at

$$\omega_p = (p + Q_{x,y})\omega_0, \quad p = n + kM, \quad (3.20)$$

where k is any integer positive or negative number and the mode number n is positive or zero. In order to study the effect of the chromaticity, the effective impedance has to be weighted by the power spectrum centred at the chromatic frequency $h_{nm}(\omega - \omega_\xi)$.

3.2.3 Collective Effects

The following sections discuss the effects due to the transverse impedance as transverse coupled-bunch instability and transverse mode coupling instability, and due to the longitudinal impedance as heat load.

Transverse Coupled-Bunch Instability

Each bunch in a multibunch beam generates a wake field. The resulting superposition of these wake fields can excite the coupled-bunch oscillations.

In a beam with M bunches the bunch-to-bunch phase shift $\Delta\phi$ is related to the coupled-bunch mode number n as $\Delta\phi = 2\pi n/M$ [35]. The transverse coupled-bunch instability (TCBI) occurs if there is a coupling between these modes.

Consider a single particle in a coasting beam, whose equation of motion is written as [38]

$$\ddot{x} + Q_{x,y}^2 \omega_0^2 x = -j \frac{e\beta}{\gamma m_0} \frac{Z_{\perp} I}{2\pi R} x, \quad (3.21)$$

where R is the synchrotron radius, and I is the beam current. The right-hand side causes the frequency shift

$$\Delta\omega = \frac{j}{2Q_{x,y}\omega_0} \frac{e\beta}{\gamma m_0} \frac{I}{2\pi R} Z_{\perp}. \quad (3.22)$$

Since the imaginary part of the complex frequency is related to the growth or decay, the growth rate of the TCBI is obtained as $\tau^{-1} = -\text{Im}\Delta\omega$.

The growth rate for the bunched beam includes a sum over the bunch spectrum. The power spectrum $h_n(\omega) = |\tilde{p}_n(\omega)|^2$ is included by reason of $Z_{\perp}(\omega)\tilde{p}_n(\omega)$ gives the deflecting field, which has to be integrated over the bunch to obtain the total force, thus

$$\Delta\omega_n = \sum_p Z_{\perp}(\omega) |\tilde{p}_n(\omega)|^2, \quad (3.23)$$

where $p_n(\omega)$ and $\tilde{p}_n(\omega)$ are standing-wave pattern and its Fourier transform. Therefore, the growth rate for the bunched beam can be written as

$$\frac{1}{\tau} = \frac{1}{1+n} \frac{1}{2Q_{x,y}\omega_0} \frac{e\beta}{\gamma m_0} \frac{I_0}{\sigma_z} Z_{\perp}^{\text{eff}}, \quad (3.24)$$

where I_0 is the bunch current. The factor $1/(1+n)$ specifies that it is more difficult to drive the higher modes [38].

As already mentioned in Sec. 3, the resistive wall impedance is of particular interest. The impedance produced by the finite resistivity of the beam pipe can be considered as the narrowband impedance. In this case only a single frequency contributes to the effective impedance $\omega_n = (n + Q_{x,y})\omega_0$, called the lowest betatron sideband [15]. Thus, Eq. 3.24 can be re-written as

$$\frac{1}{\tau} = \frac{1}{1+n} \frac{1}{2Q_{x,y}\omega_0} \frac{e\beta}{\gamma m_0} \frac{I}{2\pi R} \text{Re}(Z_{\perp}(\omega_n)) F'_m(\omega_{\xi}\sigma_{\tau} - \omega_n\sigma_{\tau}), \quad (3.25)$$

where the beam current $I = I_0 M$ with $I_0 = eN_b\omega_0/(2\pi)$ and the total number of bunch particles N_b , and the form factor

$$F'_n = \frac{2\pi R}{M\sigma_z} \frac{h_n(\omega_{\xi})}{\sum h_n(\omega)}. \quad (3.26)$$

Figure 3.4 shows the power spectrum h_n for the first four Sacherer's sinusoidal modes in the case of chromaticity $\xi = 0$.

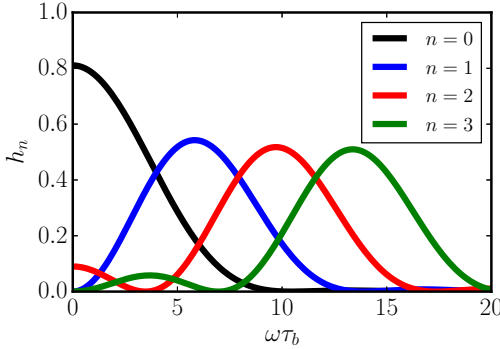


Figure 3.4: Power spectrum h_n for azimuthal modes $n = 0, 1, 2, 3$ and chromaticity $\xi = 0$.

Transverse Mode Coupling Instability

The resistive wall impedance can cause a single bunch effect such as transverse mode coupling instability (TMCI), or fast head-tail instability. This instability occurs when the increasing bunch intensity leads to the frequency shift, so the two adjacent head-tail modes overlap each other [39].

Consider the beam with short bunches. In order to find the TMCI threshold, it is possible to neglect the frequency shift of head-tail mode $m = -1$. Thus, the instability can occur if the tune shift of mode $m = 0$ equals to the synchrotron tune Q_s [40]. In other words, the beam becomes unstable when $\Delta Q = -Q_s$.

For a single bunch with the current $I = eN_b/(2\pi\sigma_\tau)$ the Eq. 3.22 can be re-written as

$$-Q_s = \frac{j}{2Q_{x,y}\omega_0} \frac{e\beta}{\gamma m_0} \frac{N_b e \omega_0}{2\pi\sigma_\tau} Z_\perp^{\text{eff}} = -\frac{e^2\beta N_b}{4\pi m_0 \gamma Q_{x,y}\sigma_\tau} \text{Im}(Z_\perp^{\text{eff}}). \quad (3.27)$$

And the intensity threshold can be expressed as

$$N_b^{\text{th}} = \frac{4\pi m_0 \gamma Q_{x,y} Q_s \sigma_\tau \omega_0}{e^2 \beta \text{Im}(Z_\perp^{\text{eff}})}. \quad (3.28)$$

3.2.4 Heat Load

The beam energy losses in the vacuum chamber can be caused by the synchrotron radiation, by the interaction with the wake fields, and by the interaction with the residual gas. The losses due the interaction with the wake fields are known as parasitic losses or heat load, measured in [W/m] [15].

A particle inside a bunch with a linear density $\lambda(\tau)$ at the time advance τ sees a decelerating voltage due to the longitudinal wake

$$V(\tau) = -e \int_{-\infty}^0 W'_0(\tau - \tau') \lambda(\tau') d\tau', \quad (3.29)$$

which results in the energy loss. For the whole bunch the energy loss is written as

$$\Delta\mathcal{E} = -e^2 \int_{-\infty}^{\tau} V(\tau) \lambda(\tau) d\tau. \quad (3.30)$$

In terms of the longitudinal impedance $Z_\parallel(\omega)$, that represents the electric field induced by the bunch, the previous equation is re-written as

$$\Delta\mathcal{E} = -2\pi e^2 N_b^2 \int_{-\infty}^{\infty} Z_\parallel(\omega) h(\omega, \sigma) d\omega. \quad (3.31)$$

In the circular machines a bunch passes through the accelerator many times, so the parasitic loss includes the contributions from the previous turns, because the power density spectrum consists of discrete lines at multiples of the angular revolution frequency ω_0 . Thus, the energy loss is presented as

$$\Delta\mathcal{E} = -2\pi e^2 N_b^2 \omega_0 \int_{-\infty}^{\infty} Z_{\parallel}(\omega) h(\omega, \sigma) d\omega. \quad (3.32)$$

It is worth to mention that the parasitic loss due to the broadband impedance is proportional to MN_b^2 . However, in case of the narrowband impedance the loss is proportional to $M^2N_b^2$ [41]. Furthermore, the heat load is directly related to the parasitic loss per length as

$$P = \frac{c\Delta\mathcal{E}}{Ct_s}, \quad (3.33)$$

where $t_s = C/M$ is the bunch spacing.

Consider a bunch of rms length σ_z and Gaussian distribution, defined by the line density $\lambda(\tau)$ and the power density $h(\omega)$ from Eq. 3.17, which moves through the cylindrical beam pipe of length $L = 2\pi R$ and generates the longitudinal resistive wall impedance Eq. 3.7. Then, the parasitic loss per revolution turn is

$$\Delta\mathcal{E} = -\frac{e^2 N_b^2 R \Gamma(\frac{3}{4})}{2\pi b \sigma_z^{3/2}} \left(\frac{Z_0 \mu_r \rho}{2c} \right)^{1/2}, \quad (3.34)$$

where $\Gamma(\frac{3}{4}) = 1.225$ is the Gamma function.

As an example, consider the parameters of the FCC-hh at injection energy from Table 1.1. Using the beam pipe radius $b \approx 12$ mm and the copper resistivity $\rho = 7.88 \times 10^{-9}$ Ωm , the average heat load per length is about 78 mW/m.

3.3 Techniques of Impedance-Induced Effects Mitigation

For the FCC-hh the planned energy is higher than for the LHC. This makes it challenging in terms of damping the instabilities, both at injection and flat top

energy. There are three main mitigation techniques that can be used in the FCC-hh:

1. Transverse feedback system (TFS) for the injection oscillation damping and the mitigation of the coupled-bunch instabilities induced by the narrowband impedance, including the resistive wall instability. TFS is a complex system, which includes the pickups to measure the beam oscillations and the kickers to damp the oscillations [7, 42]. In addition, the wide-band TFS can be used to mitigate the intra-bunch modes caused by the TMCI and electron-cloud induced instabilities. The designed feedback system supposes to provide the damping rate of 20 turns at the injection energy and 150 turns at the collision energy, which is enough to stabilise the rigid modes at chromaticity $\xi = 0$ [7].
2. Landau octupole magnets for the Landau damping [43–45]. Similar to the SPS and the LHC, the TFS in the FCC-hh will not be able to fully suppress the non-rigid modes. Therefore, the incoherent betatron tune spread, which can produce the Landau damping, can be used to mitigate the instability. In the case of LHC, 84 focusing and 84 defocusing Landau octupoles are used to produce a required betatron frequency spread for further Landau damping. In the case of FCC-hh, the number of the octupoles is much higher and not sufficient to stabilise the high order head-tail modes alone [7].
3. Electron lens [46] and RF quadrupole [47] are the alternatives to the Landau octupoles that can also produce the incoherent tune spread. For example, the electron lens promises the stronger Landau damping with less influence on the dynamic aperture in comparison to the octupoles. Nevertheless, the Landau octupoles have an advantage as they can always stabilise the beam at the expense of the increased transverse emittance. The electron lenses and RF quadrupoles can either replace the Landau octupoles or be used together with them. Both of the mentioned devices have an advantage in the size as they are only a few meters long and can save the space in the accelerator.

4 Electron Cloud Effects

This chapter discusses the phenomenon of electron cloud (EC) effect. Section 4.1 describes the generation of the primary electrons in a vacuum chamber and further production of the secondary electrons due to the secondary emission. Section 4.2 describes the EC buildup. Section 4.3 reviews the models of the secondary electron emission yield (SEY). The electron-cloud-induced effects such as heat load and energy gain in the electron cloud are described in Sec. 4.4. Possible remedies against the electron cloud induced effects are considered in Section 4.5.

4.1 Secondary Electron Emission

Secondary electron emission (SEE) occurs when a primary incident electron with sufficient energy hits a surface of a material, leading to the production of the new electrons. This complex effect was discovered in 1902 by L. Austin and H. Starke [48]. If the secondary emission yield of the pipe material, defined by the ratio between the number of emitted and impinging electrons, is greater than unity, the number of the electrons in the chamber increases exponentially with time, leading to the formation of the electron cloud (EC). The electron cloud can cause coherent instabilities, incoherent emittance growth, heat load, vacuum degradation, tune shift and spread. In order to model the electron cloud buildup, it is important to describe the production of the primary electrons (primaries) and further creation of the secondary electrons (secondaries).

Primary Electrons

The primary electrons in an accelerator are produced through following three mechanisms or their combination [49]:

1. Ionisation of the residual gas in a beam pipe. Usually residual gas is ionised by a beam leading to the production of the free electron-ion pairs. This process is always present in the beam chamber and can be dominant in the case of beams of high intensity and brightness.

-
-
2. Photoemission due to the synchrotron radiation. This mechanism occurs as a result of the emission of a significant amount of synchrotron radiation due to the high energy particle beam. The photons of the synchrotron radiation generate the primary electrons known as photoelectrons, with a corresponding photoemission yield.
 3. Production of primary electrons due to the collision of the lost beam particles with the vacuum chamber walls.

Since the third effect is usually minimised by the design, only the first two have a significant impact on the formation of EC. The contribution of photoelectrons is ignored in the EC buildup simulations due to the beam pipe geometry (Chapter 1).

Secondary Electrons

Primary electrons accelerated in the beam electromagnetic field can hit the chamber walls and generate the secondary electrons. Figure 4.1 shows the phenomenon of the secondary electrons emission. When a monokinetic electron beam of energy E_p bombards the wall, the electrons that are reflected from the wall at angles greater than 90° and without energy loss are called elastically reflected (or backscattered). The electrons that are scattered out of the material are the true secondary electrons. They appear when the primaries penetrate the material and after a few collisions, the material electrons receive the part of the primary's energy sufficient to escape [50]. However, some primaries penetrate the material and are scattered back, losing a part of the energy through several collisions. These are the rediffused electrons.

Thus, after the bombardment of the surface with the primary electrons of current I_p , the flux of secondary electrons can be categorised into three components:

1. Backscattered – elastically reflected electrons with current I_e .
2. True secondary – slow secondary electrons with current I_{ts} .
3. Rediffused – inelastically reflected electrons, i.e. primary electrons that have lost some of their energy through the interaction with the target material. These electrons have current I_r .

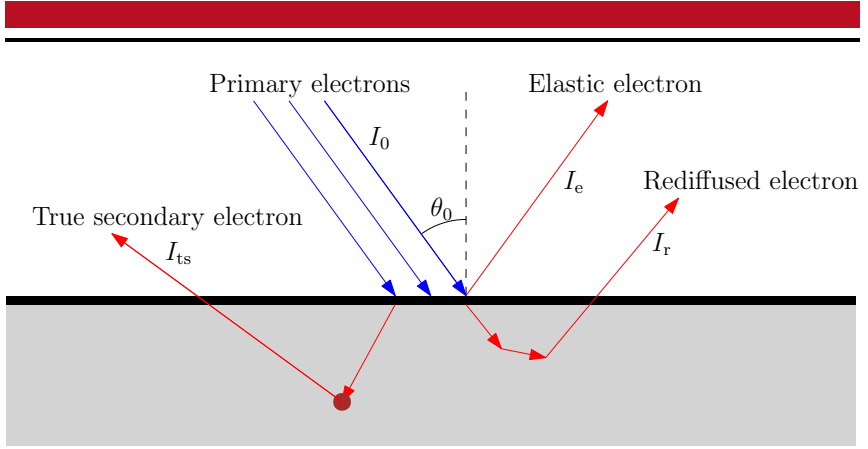


Figure 4.1.: Sketch of secondary electron emission. I_0 is the current of the incident electron and θ_0 is the incident angle, while I_{ts} , I_e , I_r correspond to the current of the true secondary, elastic and rediffused electrons, respectively.

The main quantity that describes the SEE is the total secondary emission yield

$$\delta = \frac{I_e + I_{ts} + I_r}{I_p} = \delta_e + \delta_{ts} + \delta_r, \quad (4.1)$$

where δ_e , δ_{ts} , δ_r are the emission yields for the elastic, true secondary and rediffused electrons, respectively. Since the secondary electron emission yield (SEY) is a function of the kinetic energy E_0 of the incident electron and the incident angle θ_0 , Eq. 4.1 is re-written as

$$\delta(E_0, \theta_0) = \delta_e(E_0, \theta_0) + \delta_{ts}(E_0, \theta_0) + \delta_r(E_0, \theta_0). \quad (4.2)$$

Figure 4.2 shows a typical energy distribution of the secondary electrons for the primary electron beam of energy $E_p = 300$ eV on a copper surface. The energy spectrum shows a clear separation into three parts corresponding to the three types of secondaries. It is possible to highlight two maxima. The first lays in the region with the energy $E \approx 2 - 5$ eV, and corresponds to the true secondaries. The second corresponds to the energy $E = E_p$, which corresponds to the elastic electrons.

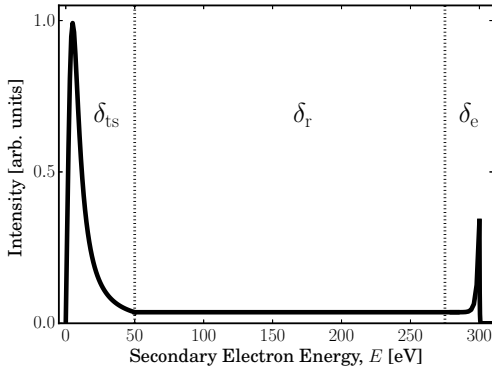


Figure 4.2.: Sketch of the energy distribution of the secondary electrons for a primary electron beam with energy $E_p = 300$ eV.

4.2 Electron Cloud Buildup

In the case of many intense bunches with a small bunch spacing, the generation of the secondary electrons can lead to the electron avalanche called beam induced multipacting. As a result of it, the electron cloud is formed. Figure 4.3 shows a buildup of an electron cloud in a beam pipe. The primary, or seed, electrons can be attracted by the beam particles, which are passing through the beam pipe. As a result, a seed electron gains an energy up to few hundred electron-volts, while the generated secondary electron has much lower energy (tens of electron-volts). Secondaries can interact with the beam pipe walls on two manners: they can either be absorbed or elastically reflected. The secondaries that are not absorbed until the next bunch can gain the energy. If these secondaries gain enough energy and accelerate towards the wall, they can produce new secondary electrons. Finally, this can cause an avalanche effect leading to the electron cloud buildup [51].

Figure 4.4 shows an example of the typical electron cloud buildup during the passage of 50 proton bunches in the presence of the external magnetic field in the case of a circular beam pipe with a radius of 20 mm. As one can see that after a certain time the density of electrons reaches the saturation level. During the EC buildup, electrons accumulate until the space charge potential of the cloud exceeds the initial kinetic energy of the secondary electrons. At the same time, new secondaries cannot penetrate the central cloud region and remain close to the pipe wall.

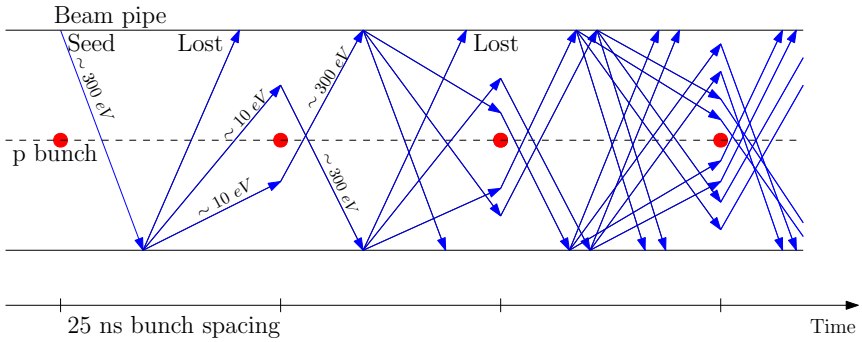


Figure 4.3.: Formation of an electron cloud in a beam pipe.

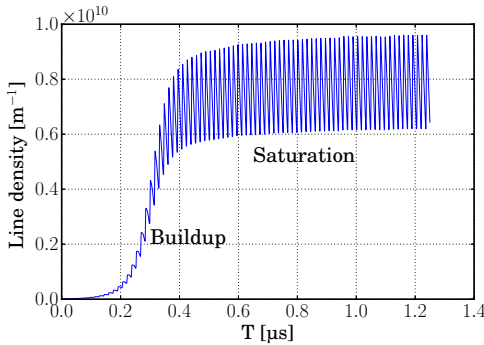


Figure 4.4.: Electron cloud buildup in 20 mm circular beam pipe, in the presence of magnetic field.

4.3 Secondary Electron Emission Yield Model

The secondary electron emission model of the beam screen surface is required in order to study the SEE related effects, such as electron cloud buildup. The SEY per incident particle and the secondary energy spectrum are the two main quantities that characterise the model. In addition, these parameters depend on the composition and surface roughness, which leads to the necessity for measurements on a surface of the used beam pipe [52].

There are many different empirical models for describing the secondary emission yield (See Refs. [53–59]). A comparison between different approaches is given in Refs. [60–62]. The main interest for the FCC-hh and

LHC is the SEY model for the copper, which is usually presented either by the Furman-Pivi [56] or Cimino-Collins [57, 58] approach. The parameters for these models are obtained from the fits to the measured data. One of the main difference between these two models is that unlike the Furman-Pivi model, the Cimino-Collins model does not allocate the rediffused electrons to a separate group. Figure 4.5 shows the dependence of the SEY components on the incident electron energy for these two models in case of $\delta(E_{\max}) = \delta_{\max} = 1.7$, where E_{\max} is the peak energy. Expression details of the incident angle and energy dependence for the corresponding components of both SEY models are provided in Appendix A.

Elastic Reflection at Low Electron Energy

Since most of the secondary electrons have rather low energy, the higher elastic reflectivity leads to a longer average survival time of electrons in the beam pipe. Of particular interest is the probability that electrons will be elastically backscattered at the low energy limit. This reflection probability is determined by the coefficient known as reflectivity $R_0 = \delta_e/\delta$. The value of R_0 plays an important role in the heat load calculations [62, 63].

Various methods were implemented for measuring and fitting of the SEY at a low energy, for example in Refs. [50, 56–58]. In Refs. [50, 64–68], the measured reflectivity is rather small and tends to zero, while in Refs. [57, 58, 69] this value is around 0.8–1.0. In addition, several theoretical approaches were proposed in order to understand the physics of this process [64, 65, 70]. It should be noted that the oversimplification of some models can lead to the erroneous conclusion about the SEY at the low incident energy [64]. For example, the simplified one-dimensional model of quantum reflection can not adequately estimate the complex interaction between the electron and potential barrier of the metal surface.

The measurements at low incident energy $E_p < 1$ eV are rather challenging [64]. The high sensitivity of the electron trajectories to electric and magnetic disturbances leads to difficulties in generating a collimated aligned electron beam at low energy [66]. Moreover, the reflectivity may depend on the surface roughness, composition and δ_{\max} [56]. The discrepancy in the previously mentioned measurements can be partially explained by the different types of materials, such as pure and technical. Whereas measurements are mainly done with the pure materials, the technical materials are used in the accelerators in the presence of an electromagnetic field [55].

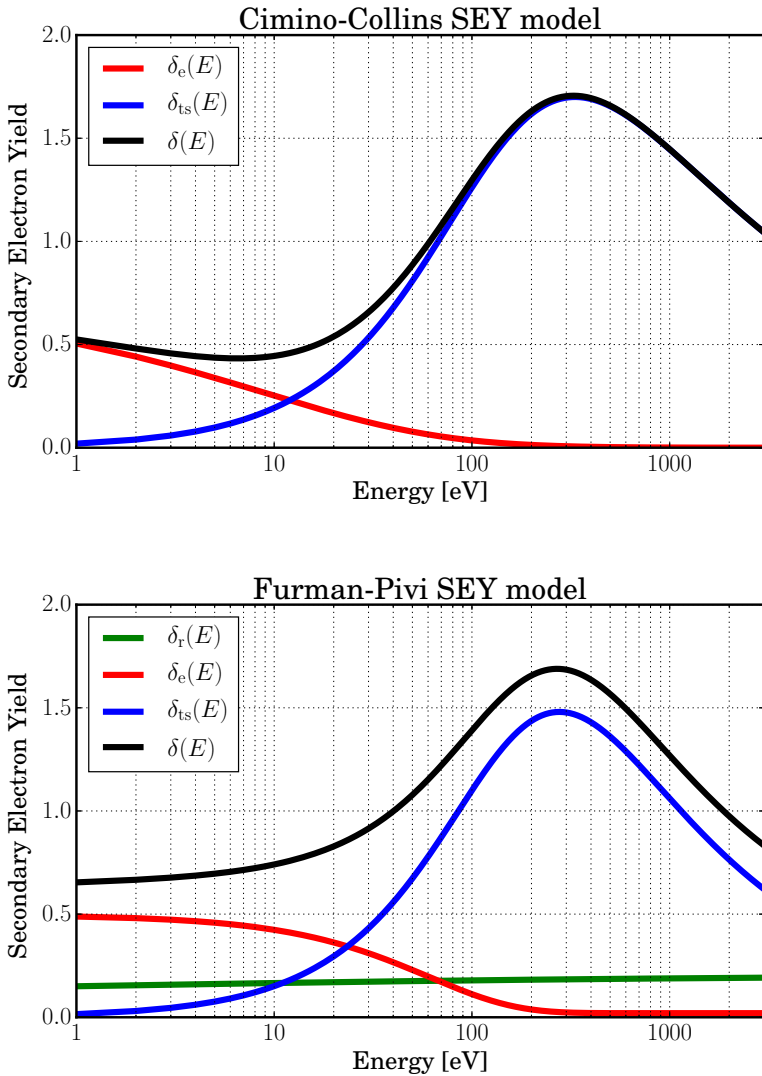


Figure 4.5.: The secondary electron emission yield for the copper for $\delta_{\max} = 1.7$ based on Cimino-Collins (top) and Furman-Pivi (bottom) fits.

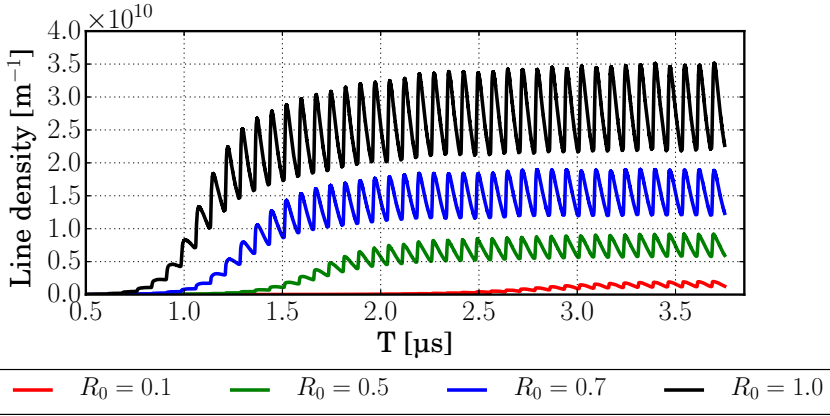


Figure 4.6.: Example of the electron density evolution in a circular beam pipe with $\delta_{\max} = 1.9$ and different values of the low-energy electron reflectivity R_0 in the presence of the dipole magnetic field.

In this thesis, the Cimino-Collins and the Furman-Pivi models are used. Figure 4.6 shows an example of the electron density evolution in the circular beam pipe using the Furman-Pivi SEY model with $\delta_{\max} = 1.9$ and different values of R_0 in the presence of the dipole magnetic field. It can be seen, the higher reflectivity leads to a higher number of stored electrons in the beam pipe with the faster electron cloud formation. Consequently, it can result in the different heat load values or SEY thresholds, leading to the wrong conclusion. Further (See Chapter 7), the reflectivity values are considered as in the published sources, that is in Cimino-Collins model $R_0 = 0.7$ and in the Furman-Pivi model $R_0 \approx 0.5$.

Rediffused Electrons

The rediffused electron yield δ_1 shows how many primary electrons come back from the material after the inelastic scattering. There is no physically meaningful distinction between the backscattered and rediffused electrons and can be rather arbitrary [56, 57]. Also, it is rather difficult to distinguish the rediffused electrons from the true secondaries at low energy. In some models both, rediffused and true secondary electrons with the energy $E_p < 50$ eV are true

secondaries [57]. Other models distinguish true and rediffused electrons by their energy, so the energy < 50 eV assigned to true secondary and the energy > 50 eV assigned to rediffused [50]. An important fact is that the energy spectrum of rediffused electrons is broad and spreads from 0 to E_p . Moreover, δ_r does not decrease for $E \rightarrow E_p$ as can be seen in Fig. 4.2 and for the case of Furman-Pivi model as shown in Fig. 4.5.

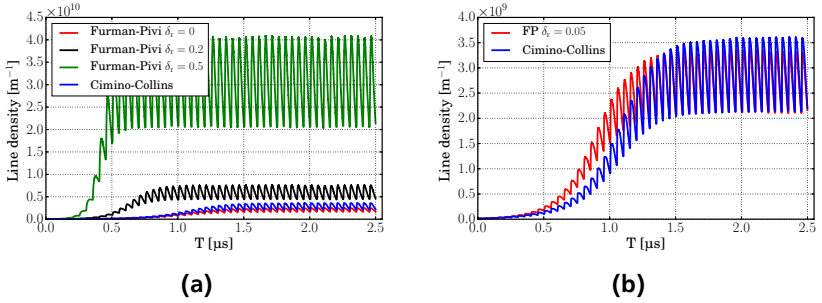


Figure 4.7.: Example of electron density evolution in the circular beam pipe for $\delta_{\max} = 1.9$ and different δ_r in Furman-Pivi SEY model in the absence of magnetic field (a). The fitting of the Furman-Pivi (“FP”) model to the Cimino-Collins model is performed with $\delta_r = 0.05$ (b).

To reveal the impact of the rediffused electrons δ_r , the simulations for the electron density evolution in the circular beam pipe are done. Since the Cimino-Collins SEY does not allocate this type of electrons into a separate group, the results with this model are treated as a reference. In the Furman-Pivi model, δ_r is adjusted at the expense of δ_{ts} , thus δ_{\max} remained fixed. The results of the EC buildup for $\delta_{\max} = 1.9$ are shown in Fig. 4.7. It can be seen that the higher fraction of the rediffused electrons leads to a higher EC density. A good agreement between two SEY models is observed in case of $\delta_r \approx 0.05$ as shown in Fig. 4.7 (b).

4.4 Electron-Cloud-Induced Effects

There are two effects that occur as a result of the interaction between the passing beam in the beam pipe and the secondary electrons. The first effect (Sec. 4.4.1) is the energy gain in the electron cloud that can be described analytically [71, 72]. The second effect (Sec. 4.4.2) is the beam energy losses due to the electron cloud known also as heat load [73].

4.4.1 Energy Gain in Electron Cloud

If the beam transfers the energy to the electrons, it can be deposited on the beam screen and leads to the additional heat load on the cryogenic system [71, 72]. The beam energy transfer, or electron cloud energy gain, is used to analyse how far the electrons are from the beam.

Assume an ultra-relativistic proton bunch which moves in the longitudinal direction z in the beam pipe as shown in Fig. 4.8. For further considerations all the magnetic effects on the electron dynamics can be omitted, because the electrons generated during the SEE are non-relativistic. Usually, the bunch length is much larger than the transverse bunch size as well as the beam pipe radius, so the energy gain in the longitudinal direction is rather small. Thus, the longitudinal direction can be neglected [72] and the equation of motion Eq. 2.1 then can be written as

$$\frac{d\vec{p}}{dt} = e\vec{E}, \quad (4.3)$$

and the momentum at a radial position r is written as

$$p = e\sigma_z E(r). \quad (4.4)$$

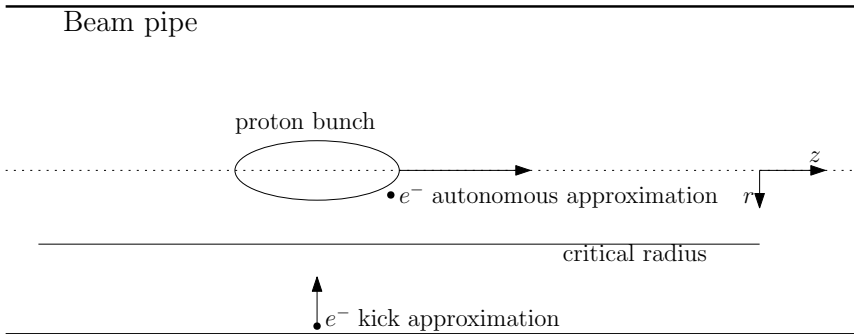


Figure 4.8.: The interaction regimes between electron and bunch according to the Berg's formalism [72].

As a result of the interaction between a bunch and electrons, two types of motion can be distinguished and described by the following approximations [72]:

1. Kick approximation: the electrons are much closer to the beam pipe walls and do not enter the bunch space.
2. Autonomous approximation: the electrons are closer to the bunch and trapped inside the bunch core. Actually, these electrons perform the harmonic oscillations since they are strongly attracted by the beam distribution.

To divide these regimes the critical radius $r_C \approx 2\sqrt{N_b r_e \sigma_z \sqrt{2/\pi}}$ is used, where r_e is the classical electron radius¹. For example, for the FCC-hh $r_C \approx 8.5$ mm, which is comparable with the beam pipe radius, and the kick approximation can be used. In case of the LHC, $r_C \approx 9$ mm, which also allows to use the kick approximation.

Consider a bunch with the constant linear charge density

$$\lambda = \frac{eN_b}{c\sigma_z}, \quad (4.5)$$

and the electric field

$$E(r) = \frac{\lambda}{2\pi\epsilon_0 r}, \quad (4.6)$$

where ϵ_0 is the vacuum permittivity. In case of the kick regime, the energy gain obtained by the electrons from a bunch is

$$\Delta E_{\text{kick}} = \frac{\Delta p^2}{2m} = 2m_e c^2 \left(\frac{N_b r_e}{b} \right)^2, \quad (4.7)$$

where the momentum Δp transferred from this bunch to the stationary electron is defined in Eq. 4.4. Here, b is the beam pipe radius.

In the autonomous regime the electrons gain the energy, which depends on the exact oscillation period, the time when a particle is exposed to the force, and the energy at the beginning of the oscillation. The oscillation frequency of electron is [74]

$$\omega_e = \sqrt{\frac{r_e \lambda c^2}{a^2}}, \quad (4.8)$$

¹ $r_e = e^2/(4\pi\epsilon_0 m_e c^2) = 2.82 \times 10^{-15}$ m

where a is the bunch radius. Thus the maximum energy gain at a distance a for the simple linear distribution is

$$\Delta E_{\text{autonomous}} = \frac{1}{2} m_e \omega_e^2 a^2 = \frac{1}{2} m_e c \frac{r_e e N_b}{\sigma_z}. \quad (4.9)$$

To obtain more accurate results for the energy gain two following assumptions can be used [71]:

- the beam distribution is Gaussian;
- the electrons in a beam pipe are not stationary and move during the bunch passage. In this case the velocity of the electrons can be computed by integrating of the equation of motion.

4.4.2 Electron-Cloud-Induced Heat Load

A bunch of protons passes through the electron cloud in the beam pipe and interacts with it through the transverse electric field. The EC electrons near the bunch are attracted towards the bunch centre or "pinched". It leads to the formation of regions with higher electron density inside the bunch [75], mainly in the bunch tail. As a result, the bunch tail generates the longitudinal electric field E_z , which is seen by the bunch head.

The energy transferred from a beam to the electrons and deposited in the beam screen is known as the heat load [72]. Thus, the heat load can be detected [51]

- locally, through the temperature rise or response from the cooling system, notably for the cryogenic system;
- globally, through the phase shift, which appears when the RF system has to compensate the beam power loss.

Similar to the heat load induced by the longitudinal resistive wall impedance (Sec. 3.2.4), the heat load caused by a bunch is written as [73]

$$\frac{dW}{ds} = -\frac{c}{t_s} \int \rho_b(\vec{r}) E_z(\vec{r}) d^3 r \approx -\frac{qc}{t_s} \int \lambda(z) E_z(z) dz, \quad (4.10)$$

where ρ_b is the bunch charge density, $E_z(z)$ is the longitudinal electric field induced by the bunch, $\lambda(z)$ is the bunch line density, t_s is the bunch spacing. The heat load is related to the stopping power S via cS/t_s [73].

The heat load per proton and per turn can also be re-written in terms of the impedance as

$$\frac{dW}{ds} = -\frac{2\pi q^2 c}{N_b L t_s} \int_{-\infty}^{\infty} Z_{\parallel}(\omega) h(\omega) d\omega, \quad (4.11)$$

where N_b is the total intensity of proton beam, and L is the beam pipe length.

In the field of the round beam with radius a , which moves in the beam pipe with radius b , the stopping power is given as the total energy gain W_e of the electrons per unit length

$$S = \frac{dW_e}{ds} = \frac{n_e}{2m_e} \int_a^b 2\pi \Delta p_{\perp}^2(r_{\perp}) r_{\perp} dr_{\perp} = \frac{r_e n_e Q_b^2}{\varepsilon_0} \ln\left(\frac{b}{a}\right), \quad (4.12)$$

where r_{\perp} is the transverse distance from bunch centre, $Q_b = qN_b$ is the total bunch charge, and the density of the homogeneous, saturated electron cloud [76]

$$n_e \approx \frac{4\varepsilon_0 E_e}{e^2 b^2}, \quad (4.13)$$

where E_e is the initial kinetic energy of the secondary electrons.

4.5 Techniques of Electron Cloud Mitigation

In order to prevent the electron cloud formation, a number of mitigation techniques are used in the particle accelerators. They can be divided into two groups:

1. Active methods based on the introduction of the external electric or magnetic fields:
 - weak longitudinal solenoid field allowing to constrain the electrons near the beam pipe walls, which in turn reduces the electron cloud density in the field-free regions [77];

-
- electrodes, absorbing or repelling the electrons through the static electric field, and reducing the density of electrons. However, the electrodes can affect the impedance. In addition, it can be challenging to find a space for them [78].
2. Passive methods that are based on the beam options and surface modifications, such as surface properties and geometrical changes:
- reduction of SEY with the coating, such as amorphous carbon (a-C) and non-evaporable getter, which allows suppressing the electron cloud buildup completely [79, 80]. The current FCC-hh impedance model considers the amorphous carbon as a default coating and it will be applied to the upper and lower parts of the beam screen [7];
 - geometrical modification such as grooves, which may act as electron traps and absorb the electrons generated by other secondaries when they hit the groove [81]. For example, the laser-treated beam screen surface is considered as an alternative to the a-C coating in the FCC-hh [7]. Laser ablation surface engineering (LASE) is a technique which can enhance the material roughness and may affect the impedance. In addition, the saw-tooth surface on the FCC-hh secondary chamber will be imprinted to reduce the amount of the photoelectrons;
 - a “scrubbing” effect, which constitutes in lowering the SEY of the beam screen surface by electron bombarding the surface, which removes the few first monolayers [82]. Unlike the LHC, scrubbing is not considered as a mitigation technique for the FCC-hh due to its large time consumption;
 - a beam filling pattern, which can help to minimise the electron density, however the EC will not be fully suppressed. The additional electron cloud study has been done for the 12.5 ns and 5 ns bunch spacing options [83]. The SEY thresholds for both options can require a surface with the SEY lower than 1.0, which is smaller than for the designed 25 ns. Concerning the number of the bunches and empty bunches in the train, the study in Ref. [83] showed that there is an insignificant reduction of the SEY in the dipoles and quadrupoles due to the increased gaps between bunch trains.

5 Simulation Tools and Methods

This chapter gives the brief overview of the simulation tools and methods used in this thesis. The finite element frequency-domain solver `BeamImpedance2D` is introduced in Sec. 5.1. Section 5.2 deals with the particle-in-cell code `openECLOUD` to study the electron cloud buildup. Section 5.3 presents a semi-analytic two-dimensional tracking tool `pySimEC`, which is developed in order to study the electron cloud buildup in the circular beam pipe.

5.1 `BeamImpedance2D`

`BeamImpedance2D` (BI2D) [84] is a two-dimensional computation tool for the transverse and longitudinal impedance, based on the finite element method. The advantage of this tool is in the ability to use it for arbitrary geometry and arbitrary frequency. Thus, the impedance of the FCC-hh detailed beam screen geometry is computed using BI2D.

The basic concept of the code is to solve the curl-curl equation of the electric field in the frequency domain. This equation is solved on a mesh of the two-dimensional cross-section of interest. From the solution of the curl-curl equation is the electric field, one can obtain the transverse and longitudinal impedances from the scalar product of the electric field and source current density. The detailed implementation of code is explained in Refs. [84, 85].

To validate the BI2D code one can assume a simple case of the circular beam pipe whose analytic solution is known with thin- and thick-wall impedance approximations (Eqs. 3.6 and 3.9). Figure 5.1 shows an example of a beam pipe with radius $b = 20$ mm, material thickness $d = 200$ μm , material resistivity $\rho = 10^{-9}$ Ωm , and $\beta \rightarrow 1$. It can be seen from the plot that the results from the 2D simulations show a good agreement with the analytical solution.

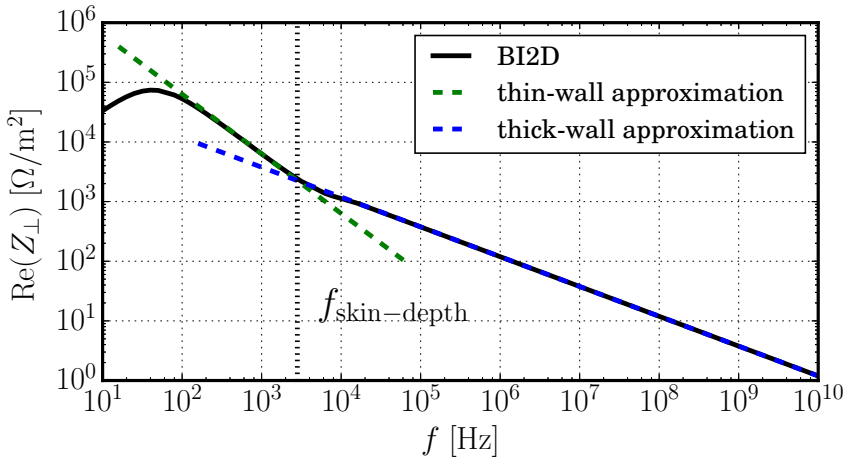


Figure 5.1.: Real part of transverse impedance per unit length of the circular beam pipe compared to analytical solution from Eqs. 3.6 and 3.9. The dashed line indicates the skin depth frequency at which the BI2D code changes its regimes.

5.2 openELOUD

openELOUD [86] is a particle-in-cell two-dimensional electrostatic code to study the electron cloud buildup in a beam pipe of arbitrary geometry. The numerical model represents the tracking of the electrons along the beam pipe, where the proton beam is located at the centre. The tracked electrons move perpendicularly to the beam direction of motion. The distribution of the transverse beam density is generated once on a 2D Cartesian grid and then scaled each time step to the local beam line density. The 2D Poisson solver is used to find the electric field. At each time step, the Poisson equation is solved for the beam density together with the electron density. To solve the Poisson equation for the transverse potential the finite integration technique cut-cell solver is implemented. Since the electrons, generated during the simulations, are described by the secondary electron emission (See Chapter 4), there are two SEY models for the copper implemented into openELOUD code: Cimino-Collins and Furman-Pivi.

Figure 5.2 shows the example of the electron distribution in the beam pipe in the absence (a) and presence (b) of the dipole magnetic field. In the field-free area, the electrons spread across the beam pipe. In a uniform magnetic field, the non-relativistic electrons follow the helicoidal trajectory around the field lines [87]. The revolution period $T = 2\pi m_e/qB$ depends on the strength of magnetic field B , which has to be taken into account in the simulations. Thus, for example, in the case of the FCC-hh flat-top energy, the magnetic field is one order higher than at the injection. As a result, it is required to increase the number of time steps. To avoid the costly computations in the case of dipole magnetic field, the drift-kinetic approximation [88] is implemented, i.e. the electrons in the beam pipe are forced to move along the magnetic dipole lines only in x- or y-direction (Fig. 5.2b).

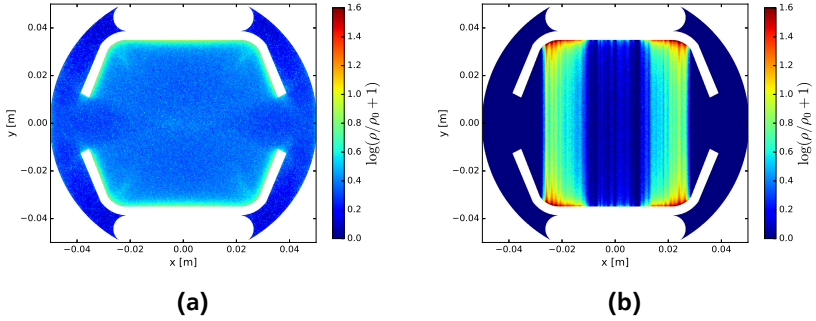


Figure 5.2.: Electron cloud distribution in the (a) absence and (b) presence of the arc dipole magnetic field.

5.3 pySimEC

The pySimEC (python Simplified Electron Cloud) is a semi-analytic two-dimensional tracking tool to study the electron cloud buildup. In order to avoid the problem with resolving a tiny beam, a circular beam pipe and a rigid bunch, which analytic solution for the electric field for the transverse profile are known, are considered. The bunch with Gaussian bunch line density $\lambda(z, t)$

(Eq. 3.17) and velocity $v_0 \approx c$ travels through the beam pipe and interacts with the electrons via the transverse electric field [76]

$$E_r(r, z) = \frac{q\lambda(z, t)}{2\pi\epsilon_0 r} \left[1 - \exp\left(-\frac{r^2}{2\sigma_\perp^2}\right) \right], \quad (5.1)$$

where r is the distance from the beam pipe centre, $\sigma_\perp = a/2$ is the rms bunch radius with the beam radius a .

The tool is based on the Cimino-Collins SEY model and the binomial distribution for the electron distribution (See Ref. [56]). Further, similarly to the openELOUD, the external dipole magnetic field is implemented as a drift-kinetic approximation, so the electrons move along the dipole magnetic lines.

The advantage of the simplified model is in its less-cost computational simulations since it is enough to use fewer particles or bunches in order to have the saturated electron cloud with the same parameters as with openELOUD.

Figure 5.3 shows an example of the electron line density in comparison obtained with pySimEC. The simulations are performed for the beam pipe with radius $b = 20$ mm in presence of dipole magnetic field, and $\delta_{\max} = 1.7$

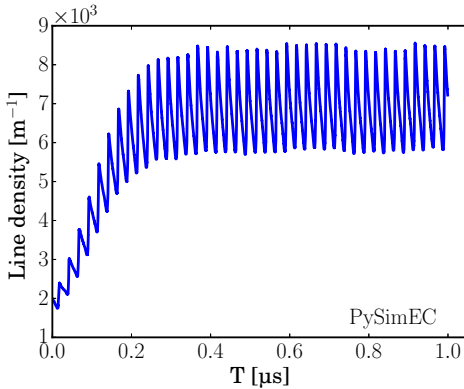


Figure 5.3: Example of the electron cloud density in the circular beam pipe with radius $b = 20$ mm in presence of dipole magnetic field, and $\delta_{\max} = 1.7$

5.4 Electron Cloud Map Formalism

The complete analysis of the electron cloud, including the secondary electrons production through the secondary emission, electron dynamics and effects in-

duced by the space charge is typically based on the costly (in terms of CPU time) computer simulations. An alternative method to study the EC buildup is the electron cloud map formalism. In Ref. [89] it was shown that for the Relativistic Heavy Ion Collider (RHIC) the electron cloud buildup, in particular, the evolution of EC density between the passage m -th and $(m + 1)$ -th bunches, can be described by a parabolic map

$$\rho_{m+1} = \alpha\rho_m + \beta\rho_m^2, \quad (5.2)$$

or by a cubic map

$$\rho_{m+1} = \alpha\rho_m + \beta\rho_m^2 + \gamma\rho_m^3. \quad (5.3)$$

Here, ρ_m is the linear electron cloud density. The parameters α, β, γ depend on the beam (such as bunch intensity, spacing, length and transverse size) and beam pipe (such as SEY details of the material surface, pipe dimensions) parameters. The linear term in Eqs. 5.2 – 5.3 defines the growth, the quadratic term describes the decay due to the saturation effects and the cubic term is related to perturbations. Using the Cimino-Collins SEY model, these terms were initially extrapolated from the simulations and the linear map coefficient α was then obtained [74]. In addition, usually it is enough to have the parabolic map to describe the electron cloud buildup.

If ρ is rather small, then Eq. 5.2 can be written as

$$\rho_m \approx \rho_0 e^{(\alpha-1)m}. \quad (5.4)$$

It can be seen that the electron cloud density grows if $\alpha > 1$ and decreases if $\alpha < 1$. However, this growth is suppressed by the space charge generated by the electrons themselves. This results in an equilibrium and hence the EC density saturation. The density of the saturated EC is defined as

$$\rho_{\text{sat}} = \begin{cases} 0 & \text{for } N < N_C \text{ or } \alpha < 1, \\ \frac{\alpha-1}{-\beta} & \text{for } N > N_C \text{ or } \alpha > 1, \end{cases} \quad (5.5)$$

where N is the bunch intensity and N_C is the bunch intensity threshold for the EC [74]. In the following section the derivation of the parameters α and β are described.

Map Coefficients

For the calculation of the map coefficients assume N_m quasi-stationary electrons are uniformly distributed in the beam pipe and gain the energy E_g during the passage of the m -th bunch (Fig. 4.3). The electrons are accelerated towards the wall after the bunch passage, and in case of the collision with the wall two new flows of electrons can be generated. The first is with energy E_g and $N_m \delta_e$ electrons which corresponds to the elastically reflected electrons. The second is with a low energy E_0 and $N_m \delta_{ts}$ electrons which corresponds to the true secondaries. These secondaries can have several wall collisions before $(m + 1)$ -th bunch arrives, leading to the generation of more flows. The sum of all these flows is a total number of the survived electrons N_{m+1} [74, 90].

If the number of electrons increases with each passage of the bunch and $N_{m+1}/N_m > 1$ holds, the electron cloud will be formed through the multipacting effect. If N_m and N_{m+1} are rather small, the growth of the number of electrons after the passage of m -th bunch is:

$$N_{m+1} = \alpha^m N_0, \quad (5.6)$$

where

$$\alpha = N_{m+1}/N_m. \quad (5.7)$$

Consider the circular beam pipe of the radius b and the electron motion limited to the transverse radial direction. The average time of flight can be written as a function of energy

$$t_F = \frac{2b}{v} = \frac{2b}{\sqrt{2E_g/m_e}}, \quad (5.8)$$

where v is the electron velocity and m_e is the electron mass.

The energy gain given by the kick approximation (Eq. 4.7) is

$$E_g = 2m_e c^2 \left(\frac{N_b r_e}{b} \right)^2.$$

The elastic electrons with the energy E_g travel across the beam pipe and hit the walls. A total number of collisions between two passing bunches given by

$$n = \frac{t_s - t_F(E_g)}{t_F(E_g)}, \quad (5.9)$$

where t_s is the bunch spacing. The total number of the elastically reflected electrons at the $(m + 1)$ -th bunch passage is

$$N_e = N_m \delta_e^m(E_g). \quad (5.10)$$

At the same time the true secondary electrons generated after the first collision with the wall produce a low energy E_0 flow. In addition, there is no distinction for the true secondaries and elastic electrons in this flow, since they are generated with the same energy. Thus, after the i -th collision with the wall, the total number of electrons is

$$N_{\text{tot}} = N_m \delta_e^{i-1} \delta_{\text{ts}} \delta_{\text{sec}}^{k_i}, \quad (5.11)$$

where $\delta_{\text{sec}} = \delta_e(E_0) + \delta_{\text{ts}}(E_0)$. The number of collisions by the low energy electrons which are generated after the i -th collision of the high energy electrons with the wall is

$$k = \frac{t_{\text{sb}} - it_F(E_0)}{t_F(E_0)}. \quad (5.12)$$

The total number of the low energy electrons at the $(m + 1)$ -th bunch passage is

$$N_{\text{ts}} = N_m \delta_{\text{ts}} \sum_{i=1}^n \delta_e^{i+1} \delta_{\text{sec}}^{k_i}. \quad (5.13)$$

As a result, the total number of electrons surviving between m -th and $(m + 1)$ -th bunches is obtained by taking into account the elastic and true secondary electrons:

$$N_{m+1} = N_m \left[\delta_e^n + \delta_{\text{ts}} \sum_{i=1}^n \delta_e^{i+1} \delta_{\text{sec}}^{k_i} \right]. \quad (5.14)$$

Taking into account Eq. 5.7, the parameter α can be defined as

$$\alpha = \delta_e^n + \delta_{ts} \sum_{i=1}^n \delta_e^{i+1} \delta_{sec}^{k_i} = \delta_e^n + \delta_{ts} \delta_{sec}^\nu \frac{\delta_{sec}^{n\nu} - \delta_e^n}{\delta_{sec}^\nu - \delta_e}, \quad (5.15)$$

where $\nu = \sqrt{E_0/E_g}$. Obviously, the coefficient α can be considered as the effective secondary electron emission yield of the beam pipe wall.

The quadratic coefficient β is defined by substitution of the saturation condition into the map

$$N_{sat} = \alpha N_{sat} + \beta N_{sat}^2, \quad (5.16)$$

where

$$\beta = \frac{1 - \alpha}{N_{sat}}. \quad (5.17)$$

Using Eq. 5.15 – 5.17 the parabolic map Eq. 5.2 can now be written as

$$N_{m+1} = \alpha N_m + \frac{1 - \alpha}{N_{sat}} N_m^2. \quad (5.18)$$

The study on the map coefficient α for the FCC-hh in comparison to the LHC is presented in Sec. 7.2.

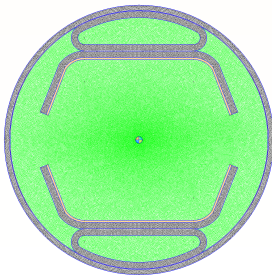
6 Beam Screen Impedance and Impedance-Induced Effects in FCC-hh

This chapter demonstrates the studies on the beam screen impedance and impedance-induced beam effects. The results of the impedance simulations and their results are discussed in Sec. 6.1, followed by the impedance-induced effects in Secs. 6.2.1 - 6.2.3. In Secs. 6.3.1- 6.3.3 the effects of different beam screen material properties, such as a-C coating, copper layer thickness and resistivity are explained.

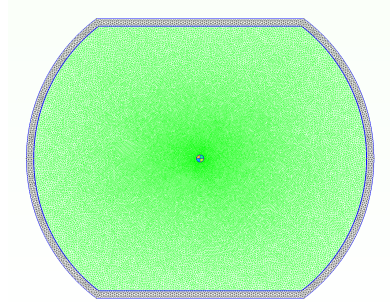
6.1 Beam Screen Impedance

The resistive wall impedances for the detailed transverse cross-sectional geometry of FCC-hh and LHC beam screens are obtained using a computational tool BI2D (see Sec. 5.1). Figure 6.1 shows the finite element method (FEM) discretisation of the FCC-hh and the LHC beam screens, respectively. The FCC-hh beam screen dimensions in the horizontal and vertical plane are considered to be 24.44 mm and 27.65 mm [7]. The current design assumes a tube with a 1 mm stainless steel of grade P506, to resist the mechanical stresses, and a 300 μm of the copper-coating layer to minimise the resistive wall losses. In comparison, the LHC beam screen diameter is 36.8 mm in the vertical plane and 46.4 mm in the horizontal plane. The LHC beam screen has also 1 mm stainless steel and a copper coating of 75 μm [31]. During the fabrication process, the elements from the copper are contaminated with the stainless steel which leads to the heterogeneous layer. To take this into account, in further simulations the thickness of copper layer in the LHC beam screen is reduced down to 50 μm (analogously to [31, 91]). The corresponding values for the resistivities of copper and stainless steel used in these calculations are listed in Table 3.1.

As already mentioned in Ch. 1, the saw-tooth pattern on the FCC-hh secondary chamber will be imprinted on copper layer with a thickness of 75 μm .



(a)



(b)

Figure 6.1.: FEM discretisation of (a) FCC-hh and (b) LHC beam screens.

However, the measurements [28] show that at low temperature the copper surface resistance is not affected by the modification in the structure. Since in further calculations only effective surface resistance is important, the saw-teeth pattern can be replaced by a smooth surface to reduce the computation complexity without significant accuracy losses. Also, the pumping holes in the beam screen can be neglected, since the design shields the beam from them [92].

The transverse impedance can be obtained with the thick-wall and thin-wall impedance approximations for the circular beam pipe from Eqs. 3.6 and 3.9, respectively. Figure 6.2 shows the transverse vertical impedance for the FCC-hh detailed beam screen geometry that is in a good agreement with these two analytic expressions, which are also shown in the figure. The analytic approximations include a single-layer material only. While the thin-wall impedance approximation is valid for high frequencies, when the material thickness is smaller than the skin depth, for lower frequencies the thick-wall impedance is used. Further in this chapter, f_{CB} denotes the coupled-bunch frequency, that is the lowest sideband frequency, and $f_{SB} = 1/\sigma_\tau$ denotes the single-bunch frequency (for the values see Table 6.1).

Using Eq. 3.6 one can predict that the vertical impedance should be higher than horizontal because of $Z \propto 1/b$, where b is the beam pipe radius. Nevertheless, from the results of BI2D calculations, for example for the flat-top energy shown in Figure 6.3, it is found that both the real and the imaginary parts of the horizontal impedance are larger than the respective parts of vertical impedance. From Fig. 6.4 one can notice the peaks in the electric field

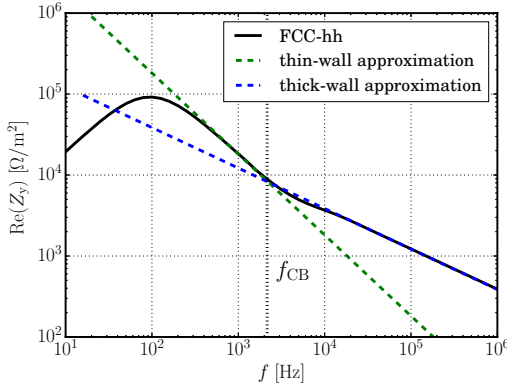


Figure 6.2.: The transverse vertical impedance per unit length at injection energy for the FCC-hh in comparison to the analytic approximations.

that correspond to the edges of the slit in the beam screen. This observation can be explained by the current design of FCC-hh beam screen, which does not consider a copper coating on some walls that are not facing the beam, in particular, a small area of stainless steel at the edges. Thus, the lack of copper at this place and a short distance to the secondary chamber lead to non-zero surface electromagnetic fields, which in turn affect the impedance.

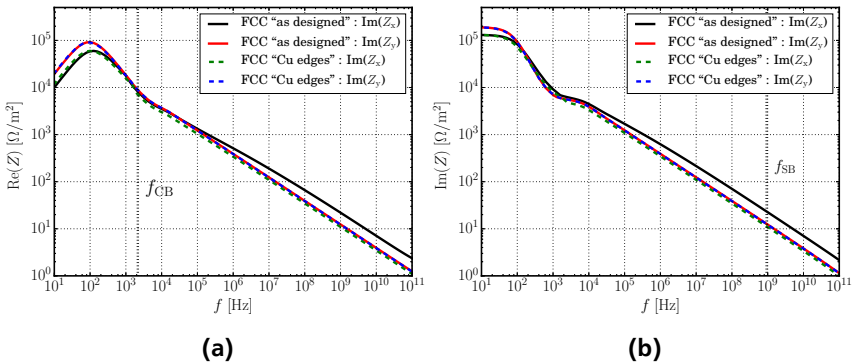


Figure 6.3.: Real (a) and imaginary (b) parts of FCC-hh transverse resistive wall impedance per unit length at the flat-top energy for the designed beam screen and beam screen with additional copper coating.

To decrease the horizontal impedance to the level of the vertical at injection energy, the additional copper coating on the edges can be applied by plasma



Figure 6.4.: Longitudinal electric field in [Vs/m] for the designed beam screen.

or cold spraying. However, the copper applied by these treatments can have different properties than the co-laminated copper [93–95]. Figure 6.5 shows the place where the additional copper is considered in the simulations. In this study, the additional copper coating is applied only on the stainless steel layer, while during the spraying procedure, the co-laminated copper will be covered as well. An extensive impedance study is conducted in order to find the optimal thickness and resistivity of additional copper coating. Thus, to reduce the horizontal impedance at injection, the thickness should be $50 - 100 \mu\text{m}$ and the resistivity should be as maximum 50% higher than the reference value, thus $\rho \approx 1.54 \times 10^{-9} \Omega\text{m}$ at the injection energy. These suggestions were considered in Ref. [96]. In the following calculations, the resistivity of all copper coatings is assumed to be equal to the co-laminated one. The transverse impedance for the case of the beam screen with the additional coating at the edges is also shown in Fig. 6.3 and is called "Cu edges".

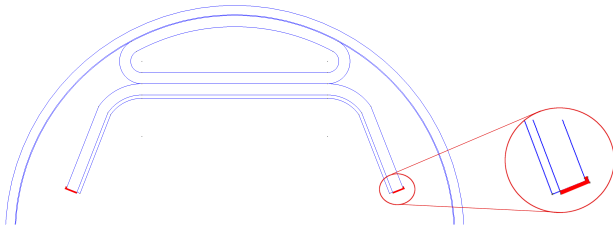


Figure 6.5.: The edges of the FCC-hh beam screen with applied additional copper coating marked with red colour. The inset shows zoom view of the coated edge.

Figure 6.6 shows the transverse impedance of FCC-hh and LHC beam screens at flat-top energy for the detailed geometries. At the flat-top energy and the

lowest betatron sideband frequency ($f_{\text{CB, FCC}} \approx 2.1$ kHz and $f_{\text{CB, LHC}} \approx 8$ kHz) the FCC-hh impedance is larger than LHC impedance by factor of 5 – 6. This difference is due to the magneto-resistivity effect (see Sec. 3.1) and beam screen size.

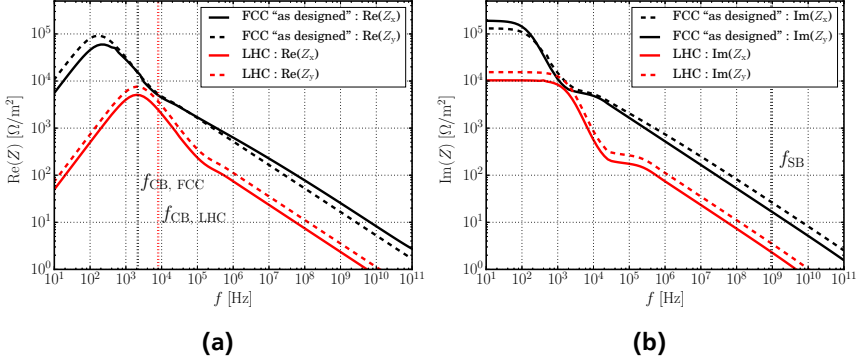


Figure 6.6.: Real (a) and imaginary (a) parts of LHC and FCC-hh transverse resistive wall impedance per unit length at the flat-top energy.

6.2 Collective Effects

This section presents the comparison of the impedance-induced effects in FCC-hh and LHC. The results for the transverse coupled-bunch instability are presented in Sec. 6.2.1, followed by the transverse mode coupling instability in Sec. 6.2.2. Section 6.2.3 covers the heat load effect.

The FCC-hh and LHC parameters that are used in the following study are summarised in Table 6.1. This thesis focuses on the scaling of beam effects with beam energy and not on the absolute estimations. Therefore, some of the values are simplified. For example, 13068 bunches in the FCC-hh are considered, whereas Table 1.1 presents the case of designed 80% of bunches in the machine. Also, the chromaticity ξ is set to zero, which considers the worst-case operation scenario.

	LHC	FCC-hh
Beam screen length, L [km]	27	100
Bunch intensity, N_b [ppb]	10^{11}	10^{11}
Number of bunches, M	2808	13068
Bunch length, σ_τ [ns]	1.08	1.07
Coupled-bunch frequency, f_{CB} [kHz]	8	2.1
Single-bunch frequency, f_{SB} [GHz]	0.93	0.93
Synchrotron tune, Q_s at E_{inj}	5.1×10^{-3}	2.8×10^{-3}
Synchrotron tune, Q_s at E_{top}	2.2×10^{-3}	1.2×10^{-3}

Table 6.1.: Parameters of the LHC and the FCC-hh used for impedance study. Here, the coupled-bunch frequency f_{CB} is the lowest sideband frequency and the single-bunch frequency is defined as $f_{SB} = 1/\sigma_\tau$.

6.2.1 Transverse Coupled-Bunch Instability

To compare the growth rate of transverse coupled-bunch instability (TCBI) between FCC-hh and LHC the scaling law is obtained using Eq. 3.25

$$\tau^{-1} \propto \frac{MN_b}{\gamma Q_{x,y}} \text{Re}(Z_\perp(f_{CB})), \quad (6.1)$$

where $Z_\perp(f_{CB})$ is the transverse impedance at the lowest betatron sideband, or coupled-bunch frequency f_{CB} .

The ratios between the growth rates for FCC-hh and LHC beam screen, obtained using the real part of the transverse impedance and the beam parameters from Table 1.1 are

$$\frac{\tau_{FCC}^{-1}}{\tau_{LHC}^{-1}} \approx \begin{cases} 3 & \text{at } E_{inj}/E_{inj}, \\ 5 & \text{at } E_{top}/E_{top}. \end{cases}$$

The growth rate of the TCBI in the FCC-hh is 3 – 5 times higher than in the LHC. As it is already mentioned in Sec. 3.3 that the designed transverse feedback system (TFS) is assumed to provide the damping rate of 20 turns at the injection energy and 150 turns at the collision energy, which is enough to

stabilise the rigid modes. Also, the Landau damping with Landau octupoles, electron lenses, and RF quadrupoles can help to damp this instability.

If the edges of the FCC-hh beam screen will be copper-coated, the impedance at f_{CB} does not undergo significant changes as can be seen from Fig. 6.3. This means that the growth rate remains the same – $\tau^{-1} \approx 100$ turns at injection energy.

The single-bunch instability can occur at frequency $f_{\text{SB}} = 1/\sigma_\tau$. Using Eq. 3.25 and applying the bunching factor $B = M\sigma_z/2\pi R$, the growth rate in this case can be written as

$$\tau^{-1} \propto \frac{N_{\text{b}}}{\gamma Q_{x,y} \sigma_z} \text{Re}(Z_{\perp}(f_{\text{SB}})). \quad (6.2)$$

In order to compare the growth rate between coupled-bunch and single-bunch instabilities, the following ratio can be used

$$\frac{\tau_{\text{CB}}^{-1}}{\tau_{\text{SB}}^{-1}} \propto \frac{MZ_{\perp}(f_{\text{CB}})}{\sigma_z Z_{\perp}(f_{\text{SB}})}. \quad (6.3)$$

The obtained ratios are a factor of 25 – 30 for the injection and flat-top energies. It means that multibunch instability is much faster than the single-bunch instability. However, assuming that the TFS (see Sec. 3.3) is strong enough to damp the multibunch instability, the growth rate can be reduced to the level of single-bunch instability [7]. Since the TFS cannot completely mitigate the single-bunch instability, Landau octupoles are required.

6.2.2 Transverse Mode Coupling Instability

For the comparison of the transverse mode coupling instability (TMCI) threshold between FCC-hh and LHC, the scaling law can be applied using the Eq. 3.25

$$N_{\text{th}} \propto \frac{\gamma \omega_0 \sigma_\tau Q_{x,y} Q_s}{\text{Im}(Z_{\perp}^{\text{eff}})}. \quad (6.4)$$

Given the imaginary part of the transverse impedance for FCC-hh and LHC and substituting the parameters from Table 1.1, the ratios are

$$\frac{N_{\text{th, FCC}}}{N_{\text{th, LHC}}} \approx \begin{cases} 0.1 & \text{at injection energy,} \\ 0.1 & \text{at flat-top energy.} \end{cases}$$

In general, the TMCI threshold due to the resistive wall is not crucial relative to other impedance sources in the machine but is still considerable. As one can see from the calculations that the TMCI threshold is ten times lower for the FCC-hh case. Taking into account the energy dependence of the FCC-hh impedance due to magnetoresistance, the threshold intensity at the flat-top energy is about five times higher than at injection energy.

Concerning the case of copper-coated edges in the FCC-hh beam screen, the TMCI threshold in the horizontal plane can be increased by a factor of 2 for both, injection and flat-top energy. In spite of this, the TMCI threshold is not affected in a vertical plane. Further increasing of TMCI threshold is possible by RF quadrupoles via the betatron frequency modulation [97].

6.2.3 Heat Load

To compare the heat load induced by the longitudinal impedance for FCC-hh and LHC beam screen, the scaling law from Eq. 3.33 is obtained as

$$P \propto \frac{\omega_0 N_b^2 \text{Re}(Z_{\parallel})}{L t_s}. \quad (6.5)$$

The heat load induced by the beam can be found by taking into account the real part of the longitudinal resistive wall impedance shown in Fig. 6.7. The influenced frequency range is limited by the revolution frequency f_0 from the left and the characteristic frequency of single bunch instabilities $f_{\text{SB}} = 1/\sigma_{\tau}$ from the right.

The ratios for the heat load between FCC-hh and LHC are

$$\frac{P_{\text{FCC}}}{P_{\text{LHC}}} \approx \begin{cases} 3.5 & \text{at injection energy,} \\ 2.4 & \text{at flat-top energy.} \end{cases}$$

From Eq. 6.5 one can observe that the higher FCC-hh heat load can be explained by the machine properties (beam pipe length and revolution fre-

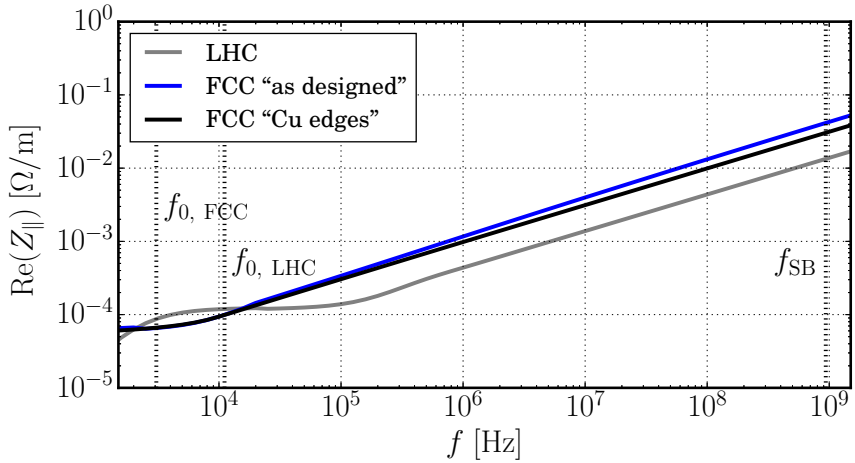


Figure 6.7.: Real part of LHC and FCC-hh longitudinal resistive wall impedance per unit length at the flat-top energy.

quency) and the longitudinal impedance, which in turn depends on the copper magnetoresistivity and beam screen size.

In the case of the copper-coated edges on the FCC-hh beam screen, the heat load can be lowered by factor

$$\frac{P_{\text{FCC}}}{P_{\text{FCC}^*}} \approx \begin{cases} 1.5 & \text{at injection energy,} \\ 1.3 & \text{at flat-top energy.} \end{cases}$$

Unlike the TMCI threshold, copper-coated edges do not significantly improve the heat load. It should be noted that the heat load in the FCC-hh is expected to be dominated by the synchrotron radiation.

During the FCC-hh design stage, two possible scenarios for the bunch spacing in the beam were considered: $t_s = 25$ ns and $t_s = 5$ ns. The effect of the bunch spacing t_s can be analysed in terms of heat load. As mentioned in Sec. 3.2.4, the heat load due to the broadband impedance is proportional to MN_b^2 , and in case of the narrowband impedance it is proportional to $M^2N_b^2$. Consider these two options with the same bunch distribution and bunch length. Using the parameters from the Table 1.1, in the case of the broadband impedance,

the switch from 25 ns to 5 ns bunch spacing leads to the heat load decrease by a factor of

$$\left(M^{(25)}\left(N_b^{(25)}\right)^2\right) / \left(M^{(5)}\left(N_b^{(5)}\right)^2\right) = 5.$$

In the case of the narrowband impedance, the heat load will not receive neither increase nor decrease as

$$\left(M^{(25)}N_b^{(25)}\right)^2 / \left(M^{(5)}N_b^{(5)}\right)^2 = 1.$$

Operating with the 5 ns bunch can help to reduce the heat load for the broad-band elements. At the same time, both options for the bunch spacing do not affect the narrowband elements. Nevertheless, using 5 ns bunch spacing requires to have a surface with $\delta_{\max} < 1$ as it was shown in the study on the SEY threshold in Ref. [83].

6.3 Effects of the Beam Screen Coating

The importance of choosing the necessary and sufficient thickness and resistivity, in particular, of the amorphous carbon (a-C) and copper coatings, is discussed in this section.

6.3.1 Amorphous Carbon Coating

The amorphous carbon coating is the baseline design option for the FCC-hh for preventing the electron cloud buildup in the machine [7]. Figure 6.8 shows the transverse vertical impedance at the flat-top energy. As can be seen, the a-C coating has a rather weak effect on the impedance if the coating thickness is small. Since the copper resistivity ($\rho \approx 10^{-9} \Omega\text{m}$) is much higher than the a-C resistivity ($\rho = 10^{-4} \Omega\text{m}$), the impedance is dominated by the copper layer. One can also notice that the impedance increase is purely imaginary in the relevant frequency range. The simulations assume the a-C coating is applied directly on the copper layer. However, the titanium sublayer on top of the copper will be used during the manufacturing process. This should not affect the impedance due to its comparable to copper resistivity. The impact on collective effects due to the a-C layer is compared with the results of the previous sections (Secs. 6.2.1 – 6.2.3).

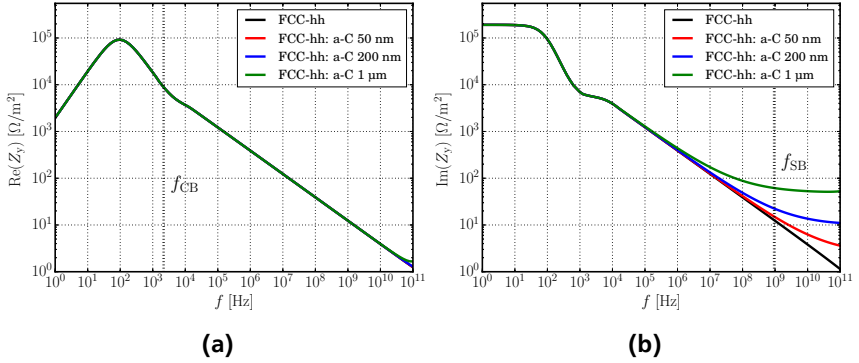


Figure 6.8.: Real (a) and imaginary (a) parts of transverse vertical resistive wall impedance at the flat-top as a function of the frequency without coating and with different thicknesses of a-C coating.

The thickness of the a-C coating required to decrease the secondary emission yield below 1.0 is approximately 30 nm which is equal to 100 – 150 carbon monolayers. However, using a thicker coating can help to avoid a material inhomogeneity, which can lead to a higher SEY [98]. Since the a-C coating affects only the imaginary part of the transverse impedance, as shown in Fig. 6.8, the TMCI threshold at injection energy for the FCC-hh in the vertical plane can be changed by the coating thickness by following factors:

$$\frac{N_{\text{th, FCC}}}{N_{\text{th, FCC+a-C}}} \approx \begin{cases} 1.0 & 50 \text{ nm coating,} \\ 1.2 & 200 \text{ nm coating,} \\ 2.4 & 1 \mu\text{m coating.} \end{cases}$$

The impact on the TMCI in the horizontal plane is negligible. It can be explained by higher horizontal impedance (see Sec. 6.1), which leads to smaller TMCI threshold in the horizontal plane. If the edges of the beam screen are covered with copper, the thresholds are increased to the level of the vertical one.

Similar to the transverse impedance, the a-C coating affects only the imaginary part of the longitudinal impedance, and the real part remains the same, as can be seen in Fig. 6.9. Consequently, the TCBI growth rate and the heat load also stay unchanged. Since the only effect that can be critical for determining

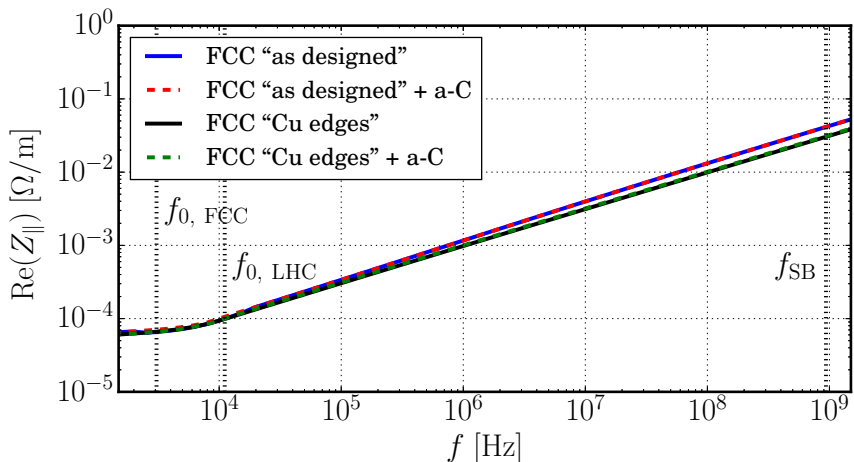


Figure 6.9.: Real part of longitudinal vertical resistive wall impedance per unit length at the flat-top as a function of the frequency in case of no coating and with different thicknesses of a-C coating.

a-C thickness is the TMCI threshold, it is recommended to use the a-C coating with the thickness below 200 nm.

Moreover, the experience of the LHC shows that there is no need to use the a-C coating along the whole beam screen. The choice of the components to be coated is based on the measured heat loads and electron cloud simulations [99].

6.3.2 Copper Coating Thickness

The transverse coupled-bunch instability is one of the crucial effects at the injection energy that occurs at the lowest betatron sideband f_{CB} . The TCBI growth rate τ^{-1} is proportional to the transverse impedance, which, in turn, depends on the material thickness and resistivity, as can be seen from the thin- and thick-wall impedance approximations (see Eqs. 3.9-3.6). The copper resistivity effect is covered in the following section.

To obtain a preliminary result on the effect of copper thickness, a simplified case of a circular beam pipe is used. Figure 6.10 shows the impedances

calculated with BI2D tool, for the circular beam pipe made of stainless steel, copper and these two layers together. The impedance of the stainless steel layer is higher at f_{CB} due to the higher resistivity of stainless steel in comparison to copper. To reduce the impedance at this frequency the effective thickness of the copper sublayer has to be found. One can obtain this thickness of $\delta \approx 300 \mu\text{m}$ by substituting the copper resistivity at the injection energy (from Table 3.1) into the formula for the skin depth (Eq. 3.8).

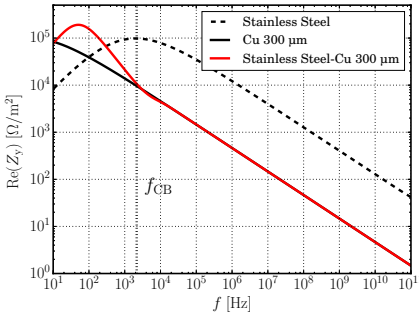


Figure 6.10.: Real part of the transverse resistive wall impedance per unit length in case of the circular beam pipe approximation of FCC-hh beam screen at injection.

Figure 6.11 shows the growth rate as a function of the copper layer thickness with the impedance obtained with BI2D tool for the detailed FCC-hh beam screen geometry, taken at the lowest betatron sideband f_{CB} . Additionally, Fig. 6.11 shows the growth rates obtained for the copper layer only from the thin-wall and the thick-wall impedance approximation. As expected for a very thin copper layer the growth rate can be described by the thin wall approximation, whereas for thick layers the thick-wall approximation holds. Moreover, the small thickness of the copper layer leads to the lower growth rate, while the high thickness leads to the saturation of the growth rate. It means that it is reasonable to use thickness at the beginning of saturation, which justifies the design choice of the copper layer thickness of $300 \mu\text{m}$.

6.3.3 Copper Coating Resistivity

The magnetoresistivity effect that depends on the temperature, strength of magnetic field, and purity of the material is discussed in Sec. 3.1. As can be seen from Eq. 3.13 the minor changes in the machine operating temperature together with the uncertainty of copper purity, lead to changes in the resistivity, which, in turn, lead to the changes in impedance. During the initial stages of the FCC-hh design, the working temperature was defined in a range

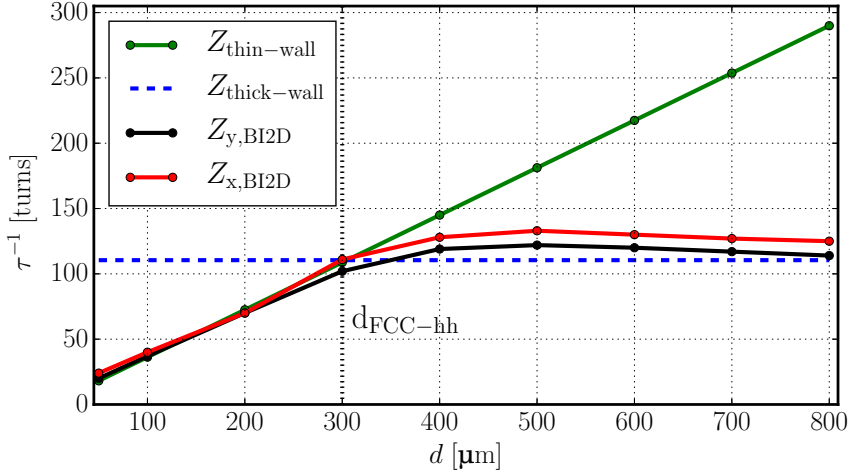


Figure 6.11.: The growth rate as a function of the copper thickness, using the thin-wall and thick-wall impedance approximations in comparison to the detailed beam screen geometry.

of 40 – 60 K with the further reference temperature of 50 K [7]. As was already mentioned in Sec. 3.1, the RRR for copper used in FCC-hh is assumed 70, similar to LHC. Despite this fact, it would be possible to have a purer copper with RRR of 100, which has to be analysed. Table 6.2 shows the values for the copper resistivity used for defining the error bars. The lowest limit is given by $\rho_{\text{RRR}=100, 40 \text{ K}}$, while the highest limit is given by $\rho_{\text{RRR}=70, 60 \text{ K}}$ [25].

RRR	T [K]	$\rho(B_0)$ [Ωm]	$\rho(B_{\text{inj}})$ [Ωm]
100	40	3.8×10^{-10}	4.2×10^{-10}
70	60	7.5×10^{-10}	1.3×10^{-9}

Table 6.2.: The copper resistivities used as the error bar limits. The magnetoresistivities are found with Kohler's rule from Eq. 3.13, where $B_{\text{inj}} = 1.06 \text{ T}$.

Figure 6.12 shows the FCC-hh transverse impedance at injection energy with the error bar defined by the uncertainties in the machine working temperature and the purity of the copper.

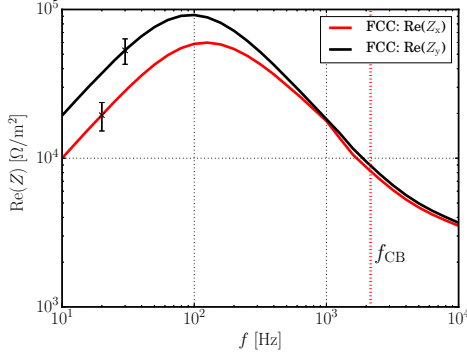


Figure 6.12.: The transverse impedance per unit length at injection energy with the corresponding error bars defined by the uncertainties in the machine working temperature and the purity of the copper.

In fact, the change in the resistivity affects the thickness of the copper coating through the skin depth effect. Using Eq. 3.8 to find the skin depth at the lowest sideband frequency f_{CB} , the corresponding values are $385 \mu\text{m}$ and $220 \mu\text{m}$ for the possible resistivities of $\rho_{RRR}=70, 60\text{K}$ and $\rho_{RRR}=100, 40\text{K}$, respectively. In comparison, the current design of the beam screen assumes the copper layer thickness of $300 \mu\text{m}$. As a result, the TMCI threshold may vary in the horizontal and vertical plane, respectively, by factors of

$$\frac{N_{\text{th,ref}}}{N_{\text{th}}} \approx \begin{cases} 1.2 \text{ and } 1.3 & \text{RRR} = 100, T = 40\text{K} \\ 0.9 \text{ and } 0.7 & \text{RRR} = 70, T = 60\text{K} \end{cases}$$

For different resistivities the TCBI growth rate ranges from 80 to approximately 135 turns, and equals to 100 turns for the designed resistivity. The TCBI growth rate can still be damped with the TFS. Unlike the TMCI threshold in the vertical plane, in the horizontal plane, it is almost unchanged. This effect can again be explained by the higher horizontal impedance and therefore, the lower TMCI threshold.



7 Electron Cloud Effects in FCC-hh

This chapter discusses the study on electron cloud (EC) effects in the FCC-hh beam screen compared to the LHC using both numerical and analytic methods. Section 7.1 presents the results on secondary electron emission yield threshold together with the electron cloud buildup. In Section 7.2 the linear map formalism is used for the analytic analysis of EC evolution. The heat load due to the electron cloud is considered in Sec. 7.3.

7.1 Secondary Electron Yield Threshold

The mitigation of EC in the FCC-hh is based on the suppression of the electron cloud buildup by reducing the emission of primary and secondary electrons. The primary electrons due to photoemission are reduced by means of beam screen design particularly through the pumping holes as shown in Fig. 1.1. The secondary electrons are preferably reduced by choosing the beam screen surface material with a low secondary electron emission. The study on the EC buildup and the secondary emission yield threshold of surface are presented in this section.

7.1.1 Electron Cloud Buildup

The electron cloud buildup simulations are performed with openECLOUD tool (See Sec. 5.2) using both Furman-Pivi and Cimino-Collins SEY models. The essential beam parameters considered for electron cloud study are listed in Table 7.1. The detailed geometry of FCC-hh and LHC beam screens are used in these simulations.

At the beginning of the simulations the density of primary electrons is considered 10^5 m^{-3} in the presence of dipole magnetic field and 10^7 m^{-3} in the absence of magnetic field. Two types of beam are considered in these simulations. First is the LHC-type beam of 4 batches with 72 bunches each and 8 empty bunches between batches. Second is the “endless” beam with no empty bunches, so all the bunches follow one by one.

Parameters, symbol [unit]	Value
Bunch intensity, N_b [ppb]	10^{11}
Bunch length, σ_z [m]	0.1
Beam size, $\sigma_{x,y}$ [mm]	1.0
Bunch spacing, t_s [ns]	25

Table 7.1.: Beam parameters for electron cloud study.

Figure 7.1 shows the examples of the EC buildup for $\delta_{\max} = 1.7$ in the case of detailed FCC-hh beam screen and circular beam pipe with radius $b = 13$ mm corresponding to average FCC-hh aperture size. The Furman-Pivi and Cimino-Collins SEY models are used to obtain the EC buildup in the presence of the arc dipole magnetic field. The electron line density increases exponentially, and then saturates due to the space charge.

The dipole magnetic field in FCC-hh is strong at both injection and flat-top energy. As a result, the EC buildup simulations at injection and flat-top energy have the same results because the electrons are forced to move along the dipole magnetic lines in both cases. It can be seen from Fig. 7.1a that the EC density from bunched and “endless” beam is the same. The EC density in the circular beam pipe (in Fig. 7.1b) is rather close to the density in the realistic geometry. Figures 7.1c and 7.1d show the EC buildup with Cimino-Collins SEY model with $\delta_{\max} = 1.7$. It can be seen from these figures that in the case of the bunched beam the electron cloud does not reach saturation after the first one or two batches. Usually, this behaviour is typical for the low SEY. At the same time, the “endless” beam is saturated at a time of the first batch pass. In the following simulations, the “endless” beam is considered with typically 200 – 250 bunches until the EC density is saturated.

Comparing the results obtained with Furman-Pivi and Cimino-Collins SEY models, one can notice that the EC density in first case is approximately 3 times higher. This effect is also discussed in Sec. 4.3, where the effects of rediffused electrons and low-energy elastic electrons reflectivity have been considered. In comparison to the Cimino-Collins model where the rediffused electrons are considered as a part of the true secondaries, the Furman-Pivi model assumes these electrons as a separate component with almost constant fraction along the electron energy spectrum. In addition, the reflective probability of elastic

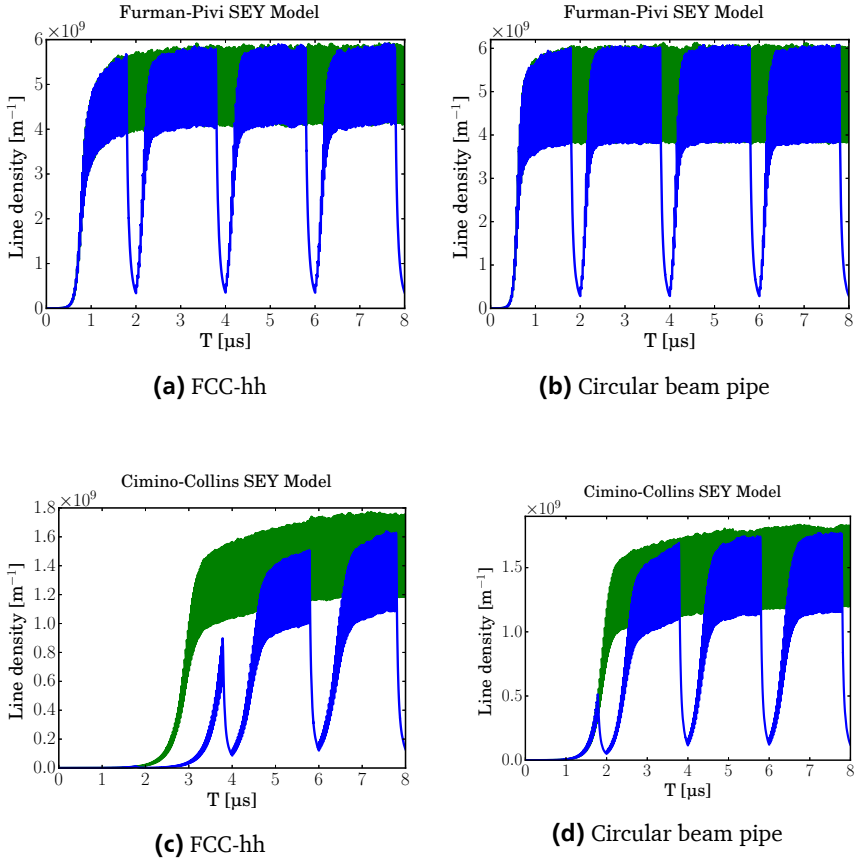


Figure 7.1.: The electron cloud buildup for $\delta_{\max} = 1.7$ in the presence of dipole magnetic field with Furman-Pivi SEY model in (a) FCC-hh beam pipe, (b) circular beam pipe. The electron cloud buildup for $\delta_{\max} = 1.7$ in the presence of dipole magnetic field with Cimino-Collins SEY model in (c) FCC-hh beam pipe, (d) circular beam pipe.

electrons at $E_0 = 0$ eV can change the simulation results due to the influence on the average survival time of the electrons in the beam pipe.

7.1.2 Secondary Electron Yield Threshold for FCC-hh and LHC

Secondary electron yield threshold is defined as a value below which the electron clouds do not saturate. It is estimated in the field-free drift and arc dipoles for both injection and flat-top energies. Figure 7.2 shows the results of the SEY thresholds for FCC-hh in comparison to LHC. The simulations are performed for the detailed beam screen geometries, which were used for impedance study. The additional case “FCC-LHC” is considered in order to investigate the effect due to the beam screen geometry. In this regard, the FCC-hh dimensions are considered together with LHC beam screen geometry.

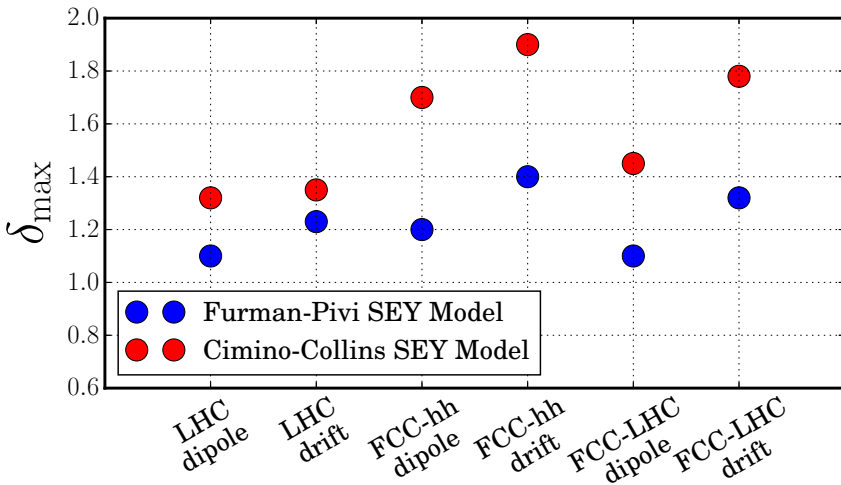


Figure 7.2.: SEY threshold δ_{\max} for LHC and FCC-hh in field-free drift and arc dipoles. Here “FCC-LHC” represents the LHC beam screen geometry with the dimensions of the FCC-hh.

The two main conclusions from these simulations are as following:

1) SEY threshold δ_{\max} shows sensitivity to employed SEY model. Comparing the results between FCC-hh and LHC, it can be seen that the SEY threshold for the FCC-hh and FCC-LHC model Cimino-Collins SEY differ significantly from the model Furman-Pivi SEY. At the same time, the LHC results do not show this behaviour. The difference between two SEY models for the FCC-hh is a factor of 0.5 and for the LHC is a factor of 0.1 – 0.2.

2) SEY threshold δ_{\max} shows sensitivity to beam screen geometry and size. Comparing FCC-hh and LHC, one can see that the results obtained with Furman-Pivi model are different by a factor about 0.2, while with Cimino-Collins model – by a factor about 0.5. Concerning the additional case “FCC-LHC”, the results are slightly different than of the complex realistic design of the beam screen. However, the difference between the SEY models is still about a factor of 0.5.

The discrepancy in the results can be explained by the different approaches in SEY models mentioned previously. The results for the SEY threshold reveal the necessity in applying the amorphous carbon on the upper and lower parts of the FCC-hh beam screen to reduce the SEY in order to prevent the electron clouds formation.

7.1.3 Secondary Emission Yield Threshold for Circular Beam Pipe

A simplified model of a circular beam pipe with average radii is used to investigate the reasons for different SEY thresholds for FCC-hh and LHC, . Figure 7.3 shows the SEY threshold δ_{\max} for circular beam pipes with the radii of 13 mm and 21 mm that correspond to the FCC-hh and the LHC cases, respectively. It can be noticed that similar to Fig. 7.2, the difference between results from two SEY models is rather large for the smaller pipe radius for both dipole field and drift. At the same time, the difference for the larger pipe radius is approximately reduced twice.

Another important parameter with large impact on the SEY is bunch intensity N_b , which needs to be considered in the simulations. Figure 7.4 shows the SEY threshold δ_{\max} as a function of bunch intensity N_b in the circular beam pipe with radius $b = 13$ mm. In the case of drift, the results with Cimino-Collins model show an increase of δ_{\max} with N_b , whereas using Furman-Pivi model δ_{\max} increases and then remains constant for $N_b > 1.5 \times 10^{11}$ protons per

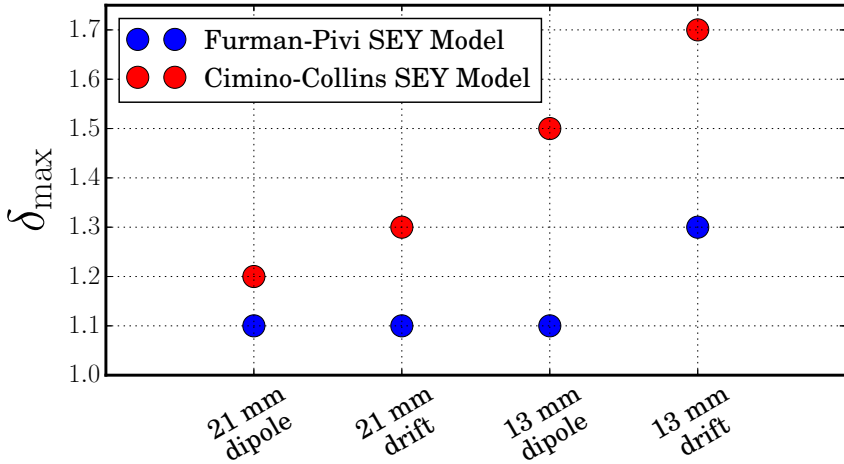


Figure 7.3.: SEY threshold for the circular beam pipe with the radii of 13 mm and 21 mm, which represent the FCC-hh and LHC cases, respectively.

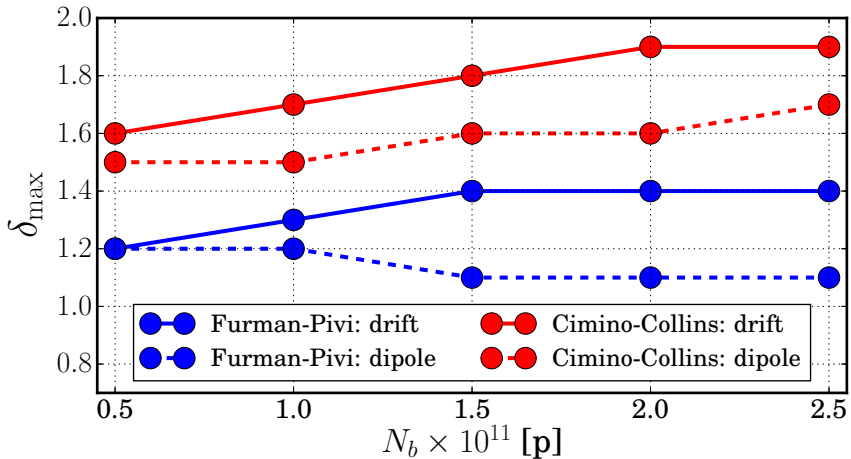


Figure 7.4.: SEY threshold as a function of bunch intensity N_b for the circular beam pipe of radius $b = 13$ mm .

bunch. Concerning the case of the magnetic dipole field, δ_{\max} shows the similar behaviour for Cimino-Collins model. However, the results with Furman-Pivi model are not that optimistic: the value of δ_{\max} decreases with N_b , and then the value also remains constant for $N_b > 1.5 \times 10^{11}$ protons per bunch. Thus, the results with Cimino-Collins model predict that the SEY threshold can be increased with the bunch intensity.

Impact of Rediffused Electrons and Elastic Electron Reflectivity

To reveal the impact from the rediffused electrons δ_r on the SEY threshold, the simulations for the circular beam pipe with radius of 20 mm are performed. Since the Cimino-Collins model does not allocate this type of electrons into a separate group, the Furman-Pivi model is used. δ_r is adjusted at the expense of δ_{ts} to fix the particular δ_{\max} . Figure 7.5 shows the SEY threshold as a function of the fraction of the rediffused electrons δ_r . The initial value of δ_r in the model is 0.2. The lower is the δ_r value, the higher is the SEY threshold. However, the SEY threshold remains constant for $\delta_r > 0.1$ in the presence of the dipole magnetic field. This effect can be explained by the electron motion in the presence of the magnetic field, since they are moving along the magnetic lines.

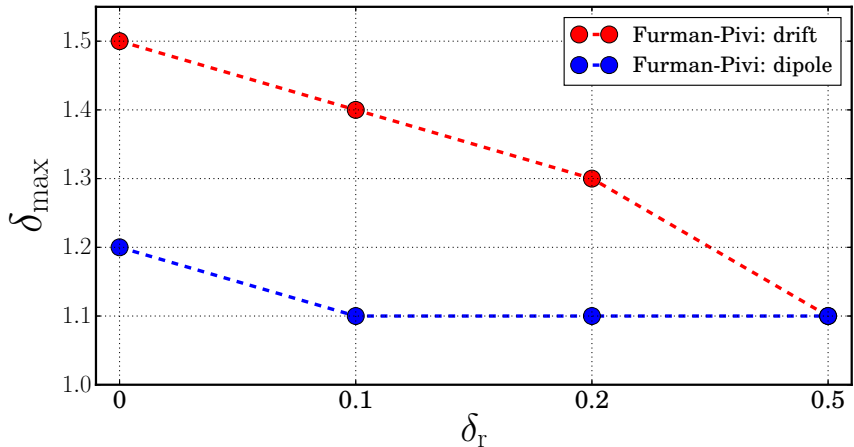


Figure 7.5.: SEY threshold δ_{\max} as a function of δ_r for the circular pipe in the absence (drift) and presence (dipole) of magnetic field.

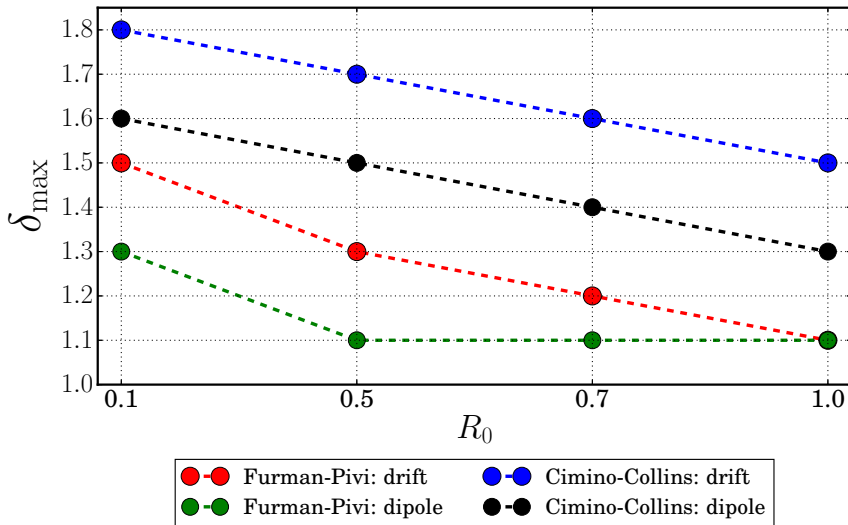


Figure 7.6.: SEY threshold δ_{\max} as a function of low-energy electron reflectivity R_0 for the circular beam pipe in the drift and arc dipoles.

Figure 7.6 shows the SEY threshold as a function of low-energy elastic electron reflectivity R_0 . Since the reflectivity R_0 defines the probability of the primary electron to scatter back from the wall, the higher reflectivity leads to the higher EC density (Fig. 4.6). As a result, it leads to faster saturation or formation of the EC. Therefore, it has lower SEY threshold. δ_{\max} shows a linear dependence on R_0 , except, the case of the present dipole magnetic field for the Furman-Pivi model, which reveals saturation for higher values of the reflectivity coefficient.

7.1.4 Energy Gain in Electron Cloud

A simple estimation of the difference between LHC and FCC-hh SEY threshold and EC buildup can be obtained using the concept of kick approximation energy gain (See Sec. 4.4.1). The maximum energy gain of an electron initially located at the pipe wall can be represented by kick approximation energy gain (Eq. 4.7), which is proportional to the beam pipe radius as

$$E_{\text{kick}} \propto \frac{1}{b^2}.$$

Substituting the corresponding values for the beam screen dimensions of FCC-hh and LHC or the corresponding average radii for circular pipe approximation. The ratios of the maximum energy gains are

$$E_{\text{kick}}^{\text{FCC}} / E_{\text{kick}}^{\text{LHC}} \approx \begin{cases} 3 & \text{for average radii,} \\ 4 & \text{for vertical half-apertures,} \end{cases}$$

where vertical half-apertures are 12.22 mm and 18.4 mm for FCC-hh and LHC, respectively. Consequently, the electrons in the beam pipe with smaller radius can be assumed to be more energetic.

Further, it is possible to assume that $\delta(E_{\text{kick}}) = \delta(E_{\text{ts}})$ [100], where the expression for $\delta(E_{\text{ts}})$ is described by Furman-Pivi or Cimino-Collins SEY model (See Appendix A). Then, the energy dependence of SEY is written as

$$\delta \propto E_{\text{kick}}^{(1-s)},$$

where $s = 1.35$ is the fitting parameter. Considering the above-obtained results for the E_{kick} ratio, one can compute

$$\delta_{\text{FCC}} / \delta_{\text{LHC}} \approx \begin{cases} 0.6 & \text{for average radii,} \\ 0.7 & \text{for vertical half-apertures.} \end{cases}$$

Consequently, it would result in a higher SEY threshold δ_{max} for FCC-hh in comparison to LHC. These results agree approximately with the results of detailed EC buildup simulations for the detailed FCC-hh and LHC beam screen geometries.

7.2 Electron Cloud Map

The evolution of electron cloud in the circular pipe in the absence of the magnetic field can be studied with the parabolic or cubic map formalism as described in Sec. 5.4. The map coefficients depend on the beam and beam pipe parameters. In the following study, only the linear map coefficient α is consid-

ered as it can help in the understanding of conditions for the EC buildup. Since this formalism is based on Cimino-Collins SEY model, the main parameters for this study can be found from its governing equations (See Appendix A). The reference and scan parameters in the study are listed in Table 7.2.

Parameters, symbol [unit]	Reference Value	Scan Range
Beam pipe radius, b [m]	...	0.01 – 0.05
Bunch intensity, $N_b \times 10^{11}$ [ppb]	1	1 – 2.5
Bunch length, σ_z [m]	0.1	...
Bunch spacing, t_s [ns]	25	...
Maximum SEY, δ_{\max}	...	0.9 – 2.1
Energy of the true secondaries, E_{sec} [eV]	2.5	...

Table 7.2.: Beam parameters used for electron cloud map analysis.

One of the main parameters used in the map formalism is the number of electron collisions with the beam pipe wall. This number is defined through the kick approximation energy gain which in turn depends on the beam pipe radius b . Then, the number of collisions can be scaled using Eq. 5.9 as

$$n \propto \frac{t_s}{b^2},$$

where t_s is the bunch spacing. Figure 7.7 shows the number of electron collisions as a function of beam pipe radius b . In the smaller beam pipe the number of electron-wall collisions is higher, so the electron survival is reduced, and the linear coefficient α is smaller than in case of the larger beam pipe. Thus, increasing the beam pipe radius, the energy gain is decreasing and, hence, the number of collisions decreases as well. For example, substituting the corresponding values for the average pipe radii of FCC-hh and LHC beam screens, one can observe that the number of electron collisions of in LHC is smaller, which leads to faster formation of electron clouds.

Figure 7.8 shows a scan of different beam and SEY parameters from Table 7.2. Since α is considered as the effective SEY, it is useful to study the conditions where $a = 1$, which determines the electron cloud buildup threshold. Figure 7.8a shows the coefficient α as a function of beam pipe radius for the bunch intensity $N_b = 10^{11}$ protons. The beam pipe with small radius produces more electron-wall collisions, so the survival of electron is reduced. Thus, the EC does not saturate in case of the beam pipe with small radius.

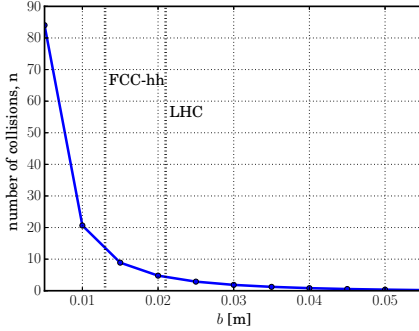
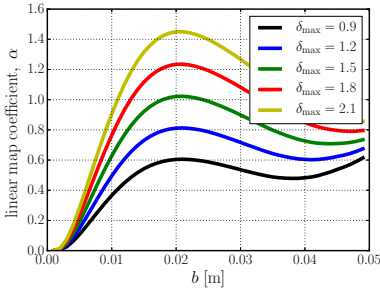


Figure 7.7.: Number of collisions as a function of beam pipe radius b .

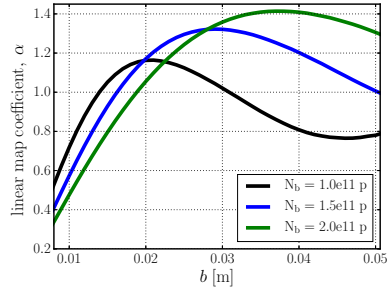
However, the SEY should be high enough to generate the electron cloud if the beam pipe is large. As one can see from Fig. 7.8a, the coefficient α reaches the maximum for beam pipe radius of 20 mm and then decreases. However, at the beam pipe radius of 50 mm it increases again. The possible explanation as follows: due to the large radius and small energy of the secondary electrons, these electrons do not have enough of energy after the collision with one pipe wall to fly to another one. So they accumulate in the beam pipe, leading again to the EC formation. Figure 7.8b demonstrates the coefficient α as a function of bunch intensity N_b and beam pipe radius b for $\delta_{\max} = 1.7$. The results show the similar nature as Fig. 7.8a.

From Fig. 7.8a one can find the SEY threshold for FCC-hh as $\delta_{\max} = 1.8 - 2.0$ and LHC as $\delta_{\max} = 1.5$. These results are rather close to the SEY threshold results obtained with openELOUD (See Figure 7.2).

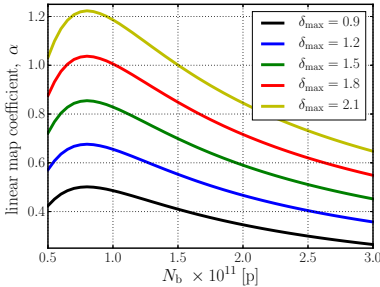
Figures 7.8c and 7.8d show the coefficient α as a function of the SEY. The coefficient α starts decay after reaching the maxima at intensity of $\approx 0.5 - 1 \times 10^{11}$ p for FCC-hh and $\approx 1 - 1.5 \times 10^{11}$ p for LHC.



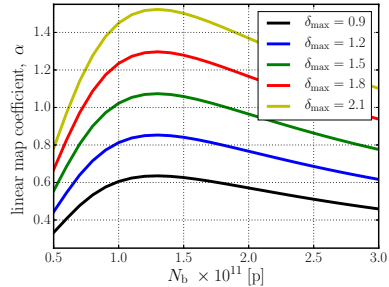
(a) Linear term α as a function of pipe radius b and SEY δ_{\max} for bunch intensity $N_b = 10^{11}$ protons per bunch.



(b) Linear term α as a function of pipe radius b and bunch intensity N_b for $\delta_{\max} = 1.7$.



(c) Linear term α as a function of (c) and (d) SEY δ_{\max} and bunch intensity N_b for FCC-hh average radius.



(d) Linear term α as a function of (c) and (d) SEY δ_{\max} and bunch intensity N_b for LHC average radius.

Figure 7.8.: Analytic prediction of the impact of the different beam and beam pipe parameters on electron cloud buildup. $\alpha = 1$ represents the threshold for electron cloud buildup.

7.3 Heat Load due to Electron Cloud

In the LHC it was observed that the electron clouds could be a source of energy loss through a dependence of the RF phase shift on the bunch spacing. In the case of FCC-hh, this effect expected to be more severe due to smaller size of the beam screen, and higher beam energy. The studies on the heat load due to EC are performed in order to gain an understanding of the scaling of EC-induced effects with beam energy and pipe size.

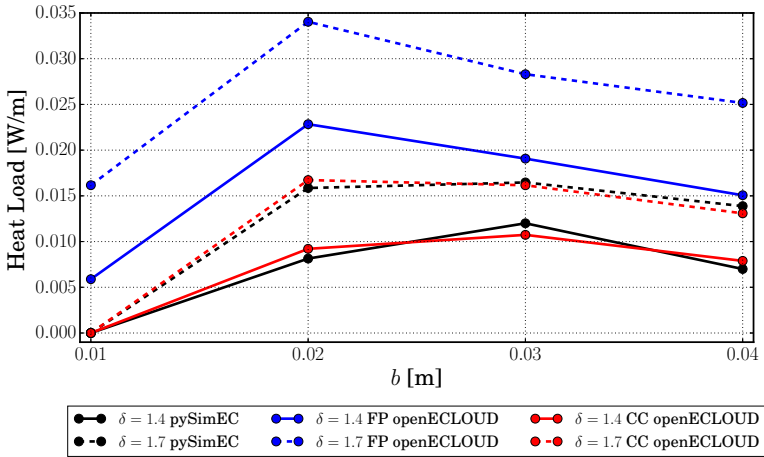


Figure 7.9.: Heat load as the function of the beam pipe radius in the presence of the dipole magnetic field. “FP” and “CC” denote the Furman-Pivi and Cimino-Collins SEY models, respectively.

openECLLOUD code is used to investigate the dependence of the EC-induced heat load on the beam pipe radius. In a PIC code, it is necessary to have a sufficient number of grid cells to resolve the electric field and the electron density across the small beam size in the large pipe. To avoid the large grid and long computation times, a semi-analytic tracking tool pySimEC is developed (See Sec. 5.3). Additionally, in the case of openECLLOUD simulations in a large beam pipe it is necessary to set the long “endless” beam with up to 350 bunches to reach the EC saturation. At the same time, in pySimEC the saturation is achievable after approximately 20 – 30 bunches.

To compare openECLLOUD and pySimEC, the simulations for the dipole magnetic field, $\delta_{\max} = 1.4$ and $\delta_{\max} = 1.7$ for beam pipe radii 10 – 40 mm are performed. Figure 7.9 shows the heat load as a function of the beam pipe radius and a beam radius of $a = 1$ mm. The openECLLOUD simulations considers both Furman-Pivi and Cimino-Collins SEY models, while the numerical model pySimEC is based on Cimino-Collins model. The results show a good agreement between semi-analytic model and numerical tool for the Cimino-Collins SEY model. As in the case of SEY thresholds, the values of the heat load from Furman-Pivi model are also higher, which can again be explained by δ_r and R_0 components.

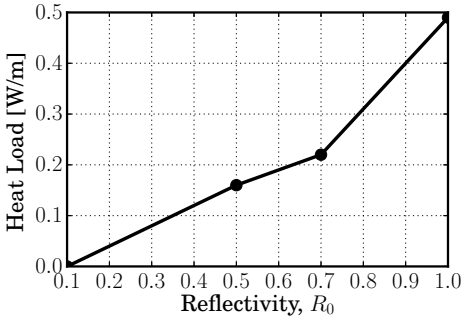


Figure 7.10.: Heat load as a function of low-energy electron reflectivity R_0 obtained with pySimEC simulations for circular beam pipe of radius 20 mm and $\delta_{\max} = 1.7$.

Figure 7.10 illustrates the heat load as a function of a low-energy elastic reflectivity R_0 performed with pySimEC tool for the circular beam pipe of radius 20 mm and $\delta_{\max} = 1.7$. It is evident that a higher value of R_0 coefficient leads to a higher heat load.

7.3.1 Heat Load Scaling with Beam Pipe Radius

The pySimEC simulations are performed to investigate the electron cloud effects dependency on the beam pipe radius b and the secondary emission yield δ_{\max} . Figure 7.11 illustrates the heat load as a function of the beam pipe radius for different δ_{\max} . The simulations are done for the pipe radii 10 – 50 mm and beam radius of $a = 1$ mm.

The heat load due to the electron cloud in the field-free region is shown in Fig. 7.11a. The higher SEY leads to the higher EC line density and, hence the higher heat load. The heat load results show a similar dependence on δ_{\max} as the linear term α from EC map. In the case of rather small pipe, the EC does

not saturate due to the reasons mentioned in Secs. 7.1.4 – 7.2. Then, the heat load reaches a maximum at $b = 20 - 30$ mm, decays, and then grows again in a rather large beam pipe. The corresponding values for the average radii of FCC-hh and LHC show that LHC has higher value of heat load. Figure 7.11b shows the results for heat load in presence of the dipole magnetic field. The results show a similar dependence as in the case of field-free region. It should be noted that presented values of heat load are per meter of length and not scaled with the fraction of length occupied in the accelerator.

As one can notice that the heat load in the drift is higher than in the dipole. This effect can be again explained by the electron motion in presence of dipole magnetic field. Since the electrons move along magnetic lines, they can not interact with the rest of the beam pipe walls. Thus, there are less new generated secondary electrons, and lower electron density, than in case of the field-free region.

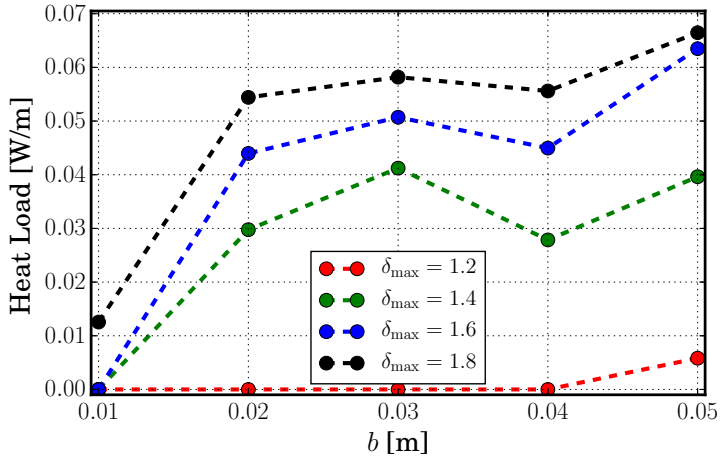
7.3.2 Heat Load Scaling with Beam Radius

The transverse betatron beam size $\sigma_{x,y}$ is related to the emittance ε , which is related to the beam energy E through

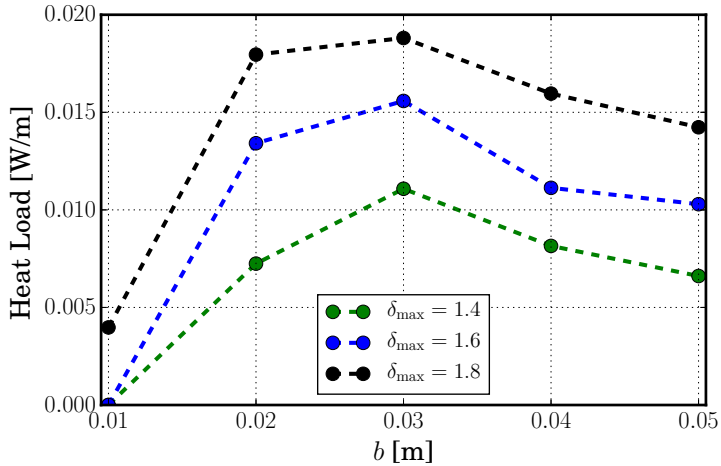
$$\sigma = \sqrt{\varepsilon\beta^*} = \sqrt{\frac{\varepsilon_n\beta^*}{\beta\gamma}} \propto \frac{1}{\sqrt{\gamma}}, \quad (7.1)$$

where $\gamma \propto E$, and $\sigma = a/2$ with the beam radius a . The normalised transverse emittance ε_n is constant. Thus, the higher beam energy leads to the shrinking of the beam. As a result, the small beam size will increase the forces between the beam and the EC at the beam centre. Therefore the EC induced effects may increase at high energy.

Here the EC buildup simulations are performed with pySimEC. Figure 7.12 shows the heat load as a function of beam radius in absence (a) and presence (b) of dipole magnetic field and δ_{\max} for beam pipe radius of 20 mm as an example. As one can notice that a small beam size, that is the higher beam energy, leads to the high heat load. Additionally, the higher SEY results in the higher EC line density. That leads to the higher heat load value.

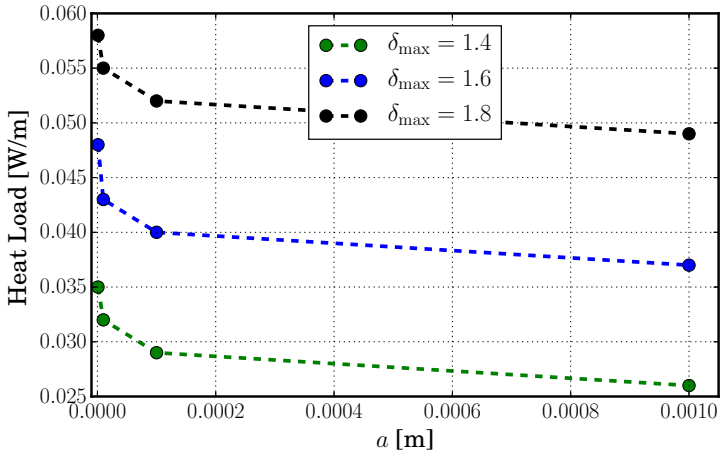


(a)

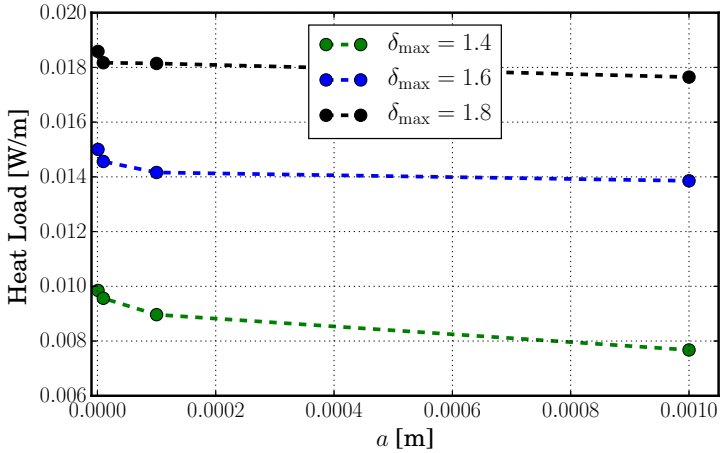


(b)

Figure 7.11.: Heat load as the function of the beam pipe radius b with beam radius of $a = 1$ mm for different values δ_{\max} in the absence (a) and presence (b) of the dipole magnetic field.



(a)



(b)

Figure 7.12.: Heat load as the function of the beam radius a in the circular beam pipe of radius $b = 20$ mm for different values δ_{\max} in the absence (a) and presence (b) of the dipole magnetic field.

7.3.3 Analytic Approach to Stopping Power

The stopping power, which is an equivalent to the heat load is obtained using an analytic approach in a field-free drift region (Sec. 4.4.2). The resulting stopping power can be written using Eq. 4.12 as

$$S = \frac{n_e r_e N_b^2}{\varepsilon_0} \ln\left(\frac{b}{a}\right), \quad (7.2)$$

where r_e is the classical electron radius, and ε_0 is the vacuum permittivity. The maximum averaged density n_e of the saturated homogeneous EC in the field-free drift section is estimated using Eq. 4.13

$$n_e = \frac{4\varepsilon_0 E_e}{e^2 b^2}, \quad (7.3)$$

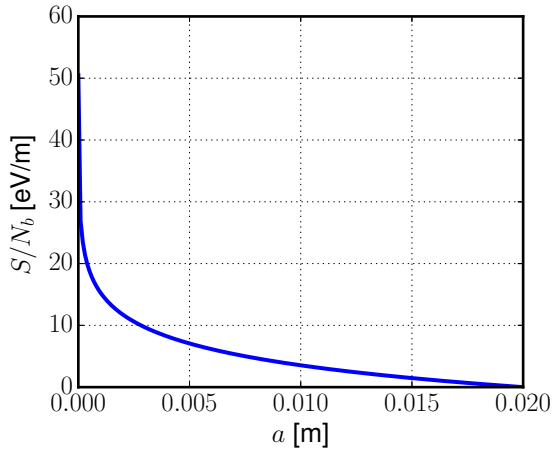
where E_e is the kinetic energy of the electrons emitted from the wall. Substituting the corresponding average radius values for FCC-hh and LHC, one can obtain that the maximum electron density for FCC-hh is about 2.5 times higher.

Figure 7.13a illustrates the stopping power as a function of the transverse beam size a . It can be seen from Eq. 7.2 that smaller beam results to the higher stopping power. These results agree with the results of the heat load scaling with beam radius (see Fig. 7.12). Figure 7.13b shows the stopping power as a function of the beam size. The smaller beam in the small beam pipe leads to the higher stopping power.

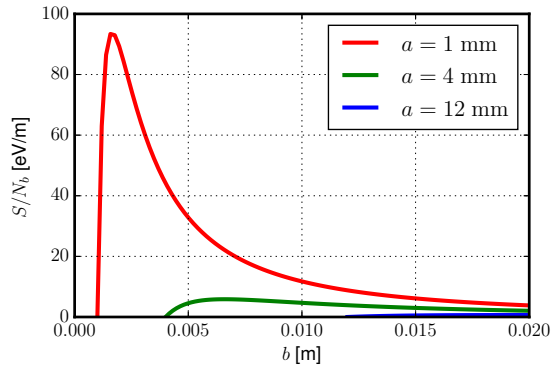
Comparing the stopping power between FCC-hh and LHC, the scaling law is used

$$S \propto \frac{1}{b^2} \ln\left(\frac{b}{a}\right).$$

For example, substituting the corresponding values for the beam energy at flat top for FCC-hh and LHC into Eq. 7.1, the beam size values are $\sigma \approx 4$ mm and $\sigma \approx 12$ mm, respectively. Further, using the FCC-hh and LHC average beam pipe radii, one can obtain the stopping power for FCC-hh that is higher by a factor of about 5 than for LHC.



(a)



(b)

Figure 7.13.: (a) Stopping power as a function of the beam radius a for beam pipe radius $b = 20$ mm. (b) Stopping power as a function of the beam pipe radius b for different beam radii a .



8 Conclusions

This thesis focuses on the scaling of collective effects with beam energy and beam screen geometry from LHC to FCC-hh. Based on the LHC experience, the FCC-hh beam screen is one of the main contributors to the collective effects. In particular, the heat load and instabilities (TCBI and TMCI) driven by beam coupling impedance and the heat load induced by electron cloud are studied.

The impedance study for the detailed geometry of the FCC-hh and LHC beam screens was performed with a 2D code based on the finite element method. Analytically, the transverse impedance was obtained by thin- and thick-wall resistive wall approximation, as well as the optimum thickness of the copper coating. The difference between FCC-hh and LHC impedances can be explained by beam screen aperture size and copper magnetoresistivity. The magnetoresistivity depends on the working temperature, purity of copper, and strength of the magnetic field. Also, the simulations of FCC-hh impedance showed that in the high-frequency range, the horizontal impedance is larger than the vertical impedance in both real and imaginary parts. Since the increased impedance lowers the TMCI threshold, this thesis work proposes modifications in the beam screen design to mitigate its impedance contribution.

This thesis also took into account the uncertainty in the copper purity and working machine temperature in the FCC-hh, which provides the margins for the transverse impedance and collective effects. In the worst-case scenario, the TCBI growth rate lies still within the working range of the transverse feedback system. In contrast, the TMCI threshold decreases due to higher impedance.

The beam energy of FCC-hh is one order of magnitude higher at both injection and flat-top in comparison to the LHC. As a result, the TCBI growth rates are only a few times lower, whereas the TMCI threshold is one order of magnitude lower for FCC-hh. As for the heat load, it is a few times higher for FCC-hh. However, it is not significant compared to the expected heat load due to synchrotron radiation.

The electron cloud buildup simulations were performed for the detailed transverse cross-section of FCC-hh and LHC beam screens using the 2D particle-in-cell code, which includes two SEY models for copper. Based on the simulation results, the SEY thresholds for the field-free region and arc dipoles were determined. The SEY threshold is sensitive to the employed SEY model and the beam screen size. Also, the SEY threshold for the field-free region obtained

with the EC map method for a circular beam pipe shows a good agreement with the results obtained for the detailed geometry. In order to mitigate the effects driven by the electron cloud, it is required to apply the amorphous carbon coating on the FCC-hh beam screen in arc dipoles.

Comparing FCC-hh and LHC, the smaller beam screen aperture in the FCC-hh potentially increases the SEY threshold. To explain this difference, the kick approximation energy gain was assumed. In the beam pipe with a small radius, the electrons can be assumed to be more energetic and have more collisions, so the survival of electrons is reduced.

A study of the heat load induced by electron cloud was conducted in order to investigate the impact of the beam energy and beam pipe radius. A semi-analytic tracking code pySimEC was developed in the framework of this thesis to study electron cloud buildup in the circular beam pipe. The simulation results show that smaller beam pipe radius results in a lower heat load. Thus, a smaller beam screen of FCC-hh leads to a lower heat load compared to LHC in both cases of absence and presence of a dipole magnetic field. However, higher beam energy results in a higher heat load or stopping power. In the case of saturated EC in a field-free region, the stopping power for FCC-hh is found to be higher than for LHC.

In general, this thesis improves the understanding of the scaling of collective effects with beam energy, using the two high-energy colliders, the existing LHC and the proposed FCC-hh. The higher energy of the FCC-hh beam, as well as the smaller size and more sophisticated geometry of the beam screen, challenge the beam stability at both injection and flat-top energy. Therefore, similar to LHC, the operation of FCC-hh relies on a combination of chromaticity, feedback system and Landau octupole magnets against impedance-induced instabilities. Furthermore, the amorphous carbon coating in the inner beam screen is proposed against the electron-cloud-induced effects.

Further studies can focus on the scaling of the collective effects from LHC to FCC-hh, including the chromaticity and higher-order bunch modes. Also, the active feedback systems can be included to estimate the beam stability.

Acknowledgement

My first and sincere thanks go to Prof. Dr. Oliver Boine-Frankenheim for accepting me as a PhD student at TEMF and allowing me to join the FCC project. I am very grateful for his patience and support over the years of my work, for his constructive criticism which helped me to improve myself. I want to thank Prof. Dr. Ursula van Rienen for being the second referee in this dissertation and interesting small talks during the KWT Workshop.

I want to thank all the TEMF colleagues and former TEMF colleagues for an excellent working environment. I thank Dr. Uwe Niedermayer, whose door was always open for productive discussions on the impedance theory. I want to thank Oliver S. Haas for the stimulating discussions on the electron clouds. I thank Aamna Khan for her priceless help with this thesis and our interesting talks about everything and nothing.

I would also like to thank colleagues from the FCC project with whom we had fruitful discussions. I thank the EuroCirCol project for financial support, which allowed me to travel a lot and to participate in many conferences.

I wish to thank Prof. Oliver Boine-Frankenheim, Uwe Niedermayer, Erika Kazantseva, Aamna Khan, Aleksandr Andreev, Adrian Oeftiger, Thilo Egenolf, Vadim Gubaidulin for useful comments on this manuscript.

Finally, I would like to thank my family and friends for their continuous support and endless love.

This work is dedicated to my grandparents.



A Secondary Electron Emission Yield Models

The components of SEE in the Furman-Pivi SEY model are defined by the following expressions [56]:

- yield of elastic electrons:

$$\delta_e(E_0, \theta_0) = \delta_e(E_0, 0)[1 + e_1(1 - \cos^{e_2} \theta_0)], \quad (\text{A.1})$$

- yield of rediffused electrons:

$$\delta_r(E_0, \theta_0) = \delta_r(E_0, 0)[1 + r_1(1 - \cos^{r_2} \theta_0)], \quad (\text{A.2})$$

- yield of true secondary electrons:

$$\delta_{\text{ts}}(E_0, \theta_0) = \hat{\delta}(\theta_0) \frac{sx}{s-1+x}, \quad (\text{A.3})$$

with

$$\begin{aligned} \delta_e(E_0, 0) &= \hat{P}_{1,e}(\infty) + [\hat{P}_{1,e} - P_{1,e}(\infty)] \exp(-(|E_0 - \hat{E}_e|/W)^p/p), \\ \delta_r(E_0, 0) &= P_{1,r}(\infty) \exp(-(E_0/E_r)^r), \\ \hat{\delta}(\theta_0) &= \hat{\delta}_{\text{ts}}[1 + t_1(1 - \cos \theta_0^{t_2})], \\ \hat{E}(\theta_0) &= \hat{E}_{\text{ts}}[1 + t_3(1 - \cos \theta_0^{t_4})], \\ x &= \frac{E_0}{\hat{E}(\theta_0)}, \end{aligned}$$

where E_0 is the kinetic energy and θ_0 is the incident angle of the incident electron, $\hat{\delta}_{\text{ts}}$ is the peak value at an energy \hat{E}_{ts} , P are the emission probabilities, $e_1, e_2, r, r_1, r_2, s, t_1, t_2, t_3, t_4, W, E_{\text{ts}}, E_r, E_e$ are the fitting and measured parameters, and p is the parameter for the binomial distribution.

The Cimino-Collins SEY model [57] is described by the two components of SEE [57, 58]:

- yield of elastic electrons:

$$\delta_e(E_0) = R_0 \left(\frac{\sqrt{E} - \sqrt{E + E_0}}{\sqrt{E} + \sqrt{E + E_0}} \right)^2, \quad (\text{A.4})$$

- yield of true secondary electrons:

$$\delta_{\text{ts}}(E_0, \theta_0) = \hat{\delta}_{\text{max}}(\theta_0) \frac{sx}{s - 1 + x}, \quad (\text{A.5})$$

with

$$\begin{aligned} \hat{\delta}_{\text{max}}(\theta_0) &= \delta_{\text{max}}(0) \exp\left(\frac{1 - \cos \theta_0}{2}\right), \\ E_{\text{max}}(\theta_0) &= E_{\text{max}}(0)[1 + 0.7 \times (1 - \cos \theta_0)], \\ x &= \frac{E}{E_{\text{max}}(\theta_0)}, \end{aligned}$$

where E_0 is the kinetic energy and θ_0 is the incident angle of the incident electron, R_0 is the low-energy elastic electron reflectivity, s is the fitting parameter, δ_{max} is the maximum SEY value at the energy E_{max} , where this maximum occurs.

Unlike the Furman-Pivi model, the elastic component in Cimino-Collins model is independent of the angle of incidence.

List of Symbols

Term	Unit	Description
a	m	Beam radius
α		Linear electron cloud map coefficient
b	m	Beam pipe radius
B_{inj}	T	Dipole magnetic flux density at injection energy
B_{top}	T	Dipole magnetic flux density at flat-top energy
β		Relativistic velocity
$\beta_{x,y}$		Beta function
c	m/s	Speed of light
C	m	Synchrotron circumference
d	m	Material thickness
δ_e		Emission yield of elastic electrons
δ_{max}		Total secondary emission yield
δ_r		Emission yield of rediffused electrons
δ_{skin}	m	Skin depth
δ_{ts}		Emission yield of true secondary electrons
e	C	Charge of electron
E_{inj}	eV	Injection beam energy
E_{kick}	eV	Energy gain in kick approximation
E_{max}	eV	Relative longitudinal coordinate
E_{top}	eV	Flat-top beam energy
ϵ_0	C/(Vm)	Vacuum permittivity
ϵ_n	m	Normalized emittance
f	Hz	Frequency
f_0	Hz	Revolution frequency
f_{CB}	Hz	Lowest sideband frequency, or coupled-bunch frequency
f_{SB}	Hz	Single-bunch frequency
γ		Relativistic factor
I, I_0	A	Beam and bunch current
L	m	Beam pipe length

Term	Unit	Description
m	kg	Particle mass
m_0	kg	Rest mass
m_e	kg	Electron mass
M		Number of bunches
μ_0	Tm/A	Vacuum permeability
μ_r		Relative magnetic permeability
n		Number of electron-beam pipe wall collisions
n_e		Electron density
N_b		Bunch intensity
N_b^{th}		Bunch intensity threshold
P	W/m	Heat load
q	C	Charge of particle
Q_s		Synchrotron tune
$Q_{x,y}$		Betatron tune
r_e	m	Classical electron radius
R	m	Synchrotron radius
R_0		Low-energy elastic electron reflectivity
RRR		Residual Resistance Ratio
ρ	Ωm	Electrical resistivity
S	eV/m	Stopping power
σ_τ	s	Bunch length
σ_z	m	Bunch length
t_s	s	Bunch spacing
T	K	Temperature
τ		Growth rate
W_{\parallel}	V/(As)	Longitudinal wake function
W_{\perp}	V/(As)	Transverse wake function
$\omega_0 = 2\pi f_0$	Hz	Revolution angular frequency
x	m	Relative transversal horizontal coordinate
y	m	Relative transversal vertical coordinate
z	m	Relative longitudinal coordinate
Z_0	Ω	Vacuum impedance
Z_{\parallel}	Ω	Longitudinal beam coupling impedance
Z_{\perp}	Ω/m	Transverse beam coupling impedance
Z_{eff}	$\Omega, \Omega/\text{m}$	Effective impedance

List of Acronyms

- a-C** Amorphous Carbon.
- ATLAS** A Toroidal LHC ApparatuS.
- CERN** Conseil européen pour la recherche nucléaire.
- CMS** Compact Muon Solenoid.
- EC** Electron Cloud.
- ECE** Electron Cloud Effect.
- FCC** Future Circular Collider.
- FCC-ee** Future Circular Collider lepton-lepton.
- FCC-eh** Future Circular Collider lepton-hadron.
- FCC-hh** Future Circular Collider hadron-hadron.
- FEM** Finite Element Method.
- HE-LHC** High Energy Large Hadron Collider.
- LHC** Large Hadron Collider.
- PIC** Particle-In-Cell.
- RHIC** Relativistic Heavy Ion Collider.
- SEE** Secondary Electron Emission.
- SEY** Secondary electron Emission Yield.
- SPS** Super Proton Synchrotron.
- TCBI** Transverse Coupled-Bunch Instability.
- TFS** Transverse Feedback System.
- TMCI** Transverse Mode Coupling Instability.
- RF** Radio Frequency.
- RRR** Residual Resistance Ratio.



List of Figures

1.1. FCC-hh and LHC beam screen photos.	3
2.1. The co-moving coordinate system in an accelerator.	8
2.2. The single-particle phase space ellipse.	10
3.1. Example of the wake field generated by the beam in the vacuum beam chamber that (a) is smooth and not perfectly conducting and (b) has changes in structure.	13
3.2. Example of transverse coupled-bunch modes n for four bunches in the synchrotron.	19
3.3. Example of head-tail modes m for a single bunch in the synchrotron.	19
3.4. Power spectrum h_n for azimuthal modes $n = 0, 1, 2, 3$ and chromaticity $\xi = 0$	23
4.1. Sketch of secondary electron emission.	29
4.2. Sketch of the energy distribution of the secondary electrons for a primary electron beam with energy $E_p = 300$ eV.	30
4.3. Formation of an electron cloud in a beam pipe.	31
4.4. Electron cloud buildup in 20 mm circular beam pipe, in the presence of magnetic field.	31
4.5. The secondary electron emission yield for the copper for $\delta_{\max} = 1.7$ based on Cimino-Collins (top) and Furman-Pivi (bottom) fits.	33
4.6. Example of electron density evolution in the circular beam pipe for different values of R_0	34
4.7. Example of electron density evolution in a circular beam pipe for different values of δ_r	35
4.8. The interaction regimes between electron and bunch.	36
5.1. Real part of transverse impedance per unit length of the circular beam pipe compared to analytical solution.	42

5.2. Electron cloud distribution in the (a) absence and (b) presence of the arc dipole magnetic field.	43
5.3. Example of the electron cloud density in the circular beam pipe.	44
6.1. FEM discretisation of (a) FCC-hh and (b) LHC beam screens. . .	50
6.2. The transverse vertical impedance per unit length at injection energy for the FCC-hh in comparison to the analytic approximations.	51
6.3. Real (a) and imaginary (b) parts of FCC-hh transverse resistive wall impedance per unit length at the flat-top energy for the designed beam screen and beam screen with additional copper coating.	51
6.4. Longitudinal electric field in [Vs/m] for the designed beam screen.	52
6.5. The edges of the FCC-hh beam screen with applied additional copper coating.	52
6.6. Real (a) and imaginary (a) parts of LHC and FCC-hh transverse resistive wall impedance per unit length at the flat-top energy. .	53
6.7. Real part of LHC and FCC-hh longitudinal resistive wall impedance per unit length at the flat-top energy.	57
6.8. Real (a) and imaginary (a) parts of transverse vertical resistive wall impedance at the flat-top as a function of the frequency without coating and with different thicknesses of a-C coating. .	59
6.9. Real part of longitudinal vertical resistive wall impedance per unit length at the flat-top as a function of the frequency in case of no coating and with different thicknesses of a-C coating. . . .	60
6.10. Real part of the transverse resistive wall impedance per unit length in case of the circular beam pipe approximation of FCC-hh beam screen at injection.	61
6.11. The growth rate as a function of the copper thickness.	62
6.12. The transverse impedance per unit length at injection energy with the corresponding error bars.	63
7.1. The electron cloud buildup for $\delta_{\max} = 1.7$ in the presence of dipole magnetic field.	67
7.2. SEY threshold δ_{\max} for LHC and FCC-hh in field-free drift and arc dipoles.	68

7.3. SEY threshold for the circular beam pipe with the radii of 13 mm and 21 mm, which represent the FCC-hh and LHC cases, respectively.	70
7.4. SEY threshold as a function of bunch intensity N_b for the circular beam pipe of radius $b = 13$ mm	70
7.5. SEY threshold δ_{\max} as a function of δ_r for the circular pipe in the absence (drift) and presence (dipole) of magnetic field.	71
7.6. SEY threshold δ_{\max} as a function of low-energy electron reflectivity R_0 for the circular beam pipe in the drift and arc dipoles.	72
7.7. Number of collisions as a function of beam pipe radius b	75
7.8. Analytic prediction of the impact of the different beam and beam pipe parameters on electron cloud buildup.	76
7.9. Heat load as the function of the beam pipe radius in the presence of the dipole magnetic field.	77
7.10. Heat load as a function of low-energy electron reflectivity R_0	78
7.11. Heat load as the function of the beam pipe radius b	80
7.12. Heat load as the function of the beam radius a	81
7.13. (a) Stopping power as a function of the beam radius a for beam pipe radius $b = 20$ mm. (b) Stopping power as a function of the beam pipe radius b for different beam radii a	83



List of Tables

1.1. The key parameters of FCC-hh and LHC.	2
3.1. Resistivities for the FCC-hh and the LHC beam screen coatings.	17
6.1. Parameters of the LHC and the FCC-hh used for impedance study.	54
6.2. The copper resistivities used as the error bar limits.	62
7.1. Beam parameters for electron cloud study.	66
7.2. Beam parameters used for electron cloud map analysis.	74



Bibliography

- [1] G. Aad *et al.*, “Observation of a new particle in the search for the Standard Model Higgs boson with the ATLAS detector at the LHC,” *Physical Letters*, vol. B716, pp. 1–29, 2012. 1
- [2] S. Chatrchyan *et al.*, “Observation of a New Boson at a Mass of 125 GeV with the CMS Experiment at the LHC,” *Physical Letters*, vol. B716, pp. 30–61, 2012. 1
- [3] W. Herr and B. Muratori, “Concept of luminosity,” in *Intermediate accelerator physics. Proceedings, CERN Accelerator School, Zeuthen, Germany, September 15-26, 2003*, pp. 361–377, 2003. 1
- [4] G. Apollinari, I. Béjar Alonso, O. Brüning, M. Lamont, and L. Rossi, “High-luminosity large hadron collider (HL-LHC): Preliminary design report,” Tech. Rep. CERN-2015-005, FERMILAB-DESIGN-2015-02, Fermi National Accelerator Lab.(FNAL), Batavia, IL (United States), 2015. 1
- [5] “The European Strategy for Particle Physics Update 2013. La stratégie européenne pour la physique des particules Mise à jour 2013. 16th Session of European Strategy Council,” May 2013. 1
- [6] “Future circular collider study.” <https://fcc.web.cern.ch/>. 1
- [7] A. Abada *et al.*, “FCC-hh: The hadron collider,” *The European Physical Journal Special Topics*, vol. 228, no. 4, pp. 755–1107, 2019. 1, 2, 26, 40, 49, 55, 58, 62
- [8] M. Benedikt *et al.*, “Future Circular Collider - European Strategy Update Documents,” Tech. Rep. CERN-ACC-2019-0003, CERN, Geneva, Jan 2019. 2
- [9] M. Benedikt and F. Zimmermann, “The physics and technology of the Future Circular Collider,” *Nature Reviews Physics*, vol. 1, no. 4, pp. 238–240, 2019. 2

-
-
- [10] L. A. Gonzalez *et al.*, “Commissioning of a beam screen test bench experiment with a future circular hadron collider type synchrotron radiation beam,” *Physical Review Accelerators and Beams*, vol. 22, no. 8, p. 83201, 2019. 3
- [11] “Beam screens for the LHC beam pipes. Les conduits pour les faisceaux LHC.” May 1997. 3
- [12] F. Zimmermann *et al.*, “Beam dynamics issues in the FCC,” in *Proceedings, 57th ICFA Advanced Beam Dynamics Workshop on High-Intensity and High-Brightness Hadron Beams (HB2016): Malmö, Sweden, July 3-8, 2016*, p. WEAM5X01, 2016. 3
- [13] J. C. Maxwell, “VIII. A dynamical theory of the electromagnetic field,” *Philosophical transactions of the Royal Society of London*, no. 155, pp. 459–512, 1865. 7
- [14] S.-Y. Lee, *Accelerator physics*. World scientific publishing, 2018. 7, 8, 10, 11
- [15] K.-Y. Ng, *Physics of intensity dependent beam instabilities*. World Scientific, 2006. 8, 18, 20, 21, 22, 24
- [16] A. Chao, *Physics of collective beam instabilities in high energy accelerators*. Wiley, 1993. 8, 13, 14, 15, 18
- [17] H. Wiedemann, *Particle accelerator physics*. Springer, 2015. 8
- [18] R. D. Ruth, “Single particle dynamics in circular accelerators,” *AIP Conf. Proc.*, vol. 153, pp. 150–235, 1987. 8
- [19] S. Kheifets and B. Zotter, *Impedances and Wakes in High Energy Particle Accelerators*. World Scientific, 1998. 13, 20
- [20] L. Palumbo, V. G. Vaccaro, and M. Zobov, “Wake fields and impedance,” *arXiv preprint physics/0309023*, 2003. 14
- [21] J. Laclare, “Coasting beam longitudinal coherent instabilities,” 1994. 15
- [22] A. Koschik, “Transverse Resistive Wall Wakefunction with Inductive Bypass,” Tech. Rep. AB-Note-2003-088-ABP, CERN, Geneva, Nov 2003. 15
- [23] A. W. Chao and M. Tigner, *Handbook of Accelerator Physics and Engineering*. Singapore: World Scientific, 1999. 16

-
- [24] F. Flickett, *Electrical properties of materials and their measurement at low temperatures*. 1982. 16
- [25] E. S. Drexler, R. P. Reed, and N. J. Simon, *Properties of copper and copper alloys at cryogenic temperatures*. NIST Mono., Gaithersburg, MD: NIST, 1992. 16, 62
- [26] R. Berman and D. K. C. MacDonald, “The thermal and electrical conductivity of copper at low temperatures,” *Proceedings of the Royal Society of London. Series A, Mathematical and Physical Sciences*, vol. 211, no. 1104, pp. 122–128, 1952. 16
- [27] A. Croft, E. Faulkner, J. Hatton, and E. Seymour, “XXXI. The electrical resistivity of gold at very low temperatures,” *The London, Edinburgh, and Dublin Philosophical Magazine and Journal of Science*, vol. 44, pp. 289–296, Mar. 1953. 16
- [28] F. Caspers, M. Morvillo, F. Ruggiero, J. Tan, and H. Tsutsui, “Surface resistance measurements of LHC dipole beam screen samples,” in *Particle accelerator. Proceedings, 7th European Conference, EPAC 2000, Vienna, Austria, June 26-30, 2000. Vol. 1-3*, pp. 376–378, 2000. 16, 50
- [29] M. Kohler, “Zur magnetischen widerstandsänderung reiner metalle,” *Annalen der Physik*, vol. 424, no. 1-2, pp. 211–218, 1938. 17
- [30] E. Métral, “Beam screen issues,” *arXiv preprint arXiv:1108.1643*, 2011. 17
- [31] O. S. Bruning *et al.*, “LHC Design Report Vol.1: The LHC Main Ring,” 2004. 17, 49
- [32] D. Brandt and L. Vos, “Resistive wall instability for the LHC: intermediate review,” Tech. Rep. CERN-LHC-Project-Note-257, CERN, 2001. 17
- [33] S. Sgobba, “Materials for high vacuum technology: An overview,” in *CERN Accelerator School, vacuum in accelerators, Platja d’Aro, Spain, 16-24 May 2006*, pp. 117–143, 2006. 17
- [34] F. Ruggiero, “Single beam collective effects in the LHC,” *Part. Accel.*, vol. 50, no. CERN-SL-95-09-AP, CERN-SL-95-9-AP, CERN-LHC-NOTE-313, pp. 83–104, 1995. 17, 18
- [35] F. Pedersen, “Multibunch instabilities,” in *Frontiers of Particle Beams: Factories with e+ e-Rings*, pp. 269–292, Springer, 1994. 18, 22

-
- [36] B. Zotter, “The effective coupling impedance for bunched beam instabilities,” no. CERN-ISR-TH-78-16, 1978. 19
- [37] F. Sacherer, “Methods for computing bunched-beam instabilities,” 1972. 20
- [38] F. Sacherer, “Transverse-Part II: Bunched Beams,” in *Proceedings of 1st International School of Particle Accelerators “Ettore Majorana”, Erice, Italy*, no. CERN-1977-013, 10 - 22 Nov 1976. 22
- [39] W. Herr, “Overview-intensity limitations in particle accelerators,” *CERN Yellow Reports: School Proceedings*, vol. 3, p. 1, 2017. 23
- [40] J. Gareyte, “Transverse mode coupling instabilities,” in *AIP Conference Proceedings*, AIP, 2001. 23
- [41] M. Furman, H. Lee, and B. Zotter, “Energy Loss of Bunched Beams in SSC RF Cavities,” *Conf. Proc.*, vol. C870316, p. 1049, 1987. 25
- [42] W. Höfle *et al.*, “Transverse feedback system for the cern fcc-hh collider,” in *9th Int. Particle Accelerator Conf.(IPAC’18), Vancouver, BC, Canada, April 29-May 4, 2018*, pp. 1997–2000, JACOW Publishing, Geneva, Switzerland, 2018. 26
- [43] J. S. Berg and F. Ruggiero, “Landau damping with two-dimensional betatron tune spread,” 1996. 26
- [44] C. Tambasco *et al.*, “Landau damping studies for the fcc: Octupole magnets, electron lens and beam-beam effects,” in *9th Int. Particle Accelerator Conf.(IPAC’18), Vancouver, BC, Canada, April 29-May 4, 2018*, pp. 3150–3153, JACOW Publishing, Geneva, Switzerland, 2018. 26
- [45] V. Kornilov *et al.*, “Landau damping and tune-spread requirements for transverse beam stability,” in *9th Int. Particle Accelerator Conf.(IPAC’18), Vancouver, BC, Canada, April 29-May 4, 2018*, pp. 3168–3171, JACOW Publishing, Geneva, Switzerland, 2018. 26
- [46] V. Shiltsev, Y. Alexahin, A. Burov, and A. Valishev, “Landau damping of beam instabilities by electron lenses,” *Physical Review Letters*, vol. 119, p. 134802, Sep 2017. 26
- [47] A. Grudiev, K. Li, and M. Schenk, “Radio frequency quadrupole for landau damping in accelerators: analytical and numerical studies,” 2015. 26

-
- [48] L. Austin and H. Starke, “Ueber die reflexion der kathodenstrahlen und eine damit verbundene neue erscheinung secundärer emission,” *Annalen der Physik*, vol. 314, no. 10, pp. 271–292, 1902. 27
- [49] G. Rumolo and G. Iadarola, “Electron clouds,” *CERN Yellow Reports: School Proceedings*, vol. 3, p. 411, 2017. 27
- [50] I. Bronshtein and B. Fraiman, *Vtorichnaya elektronnaya emissiya. (Secondary Electron Emission)*. Nauka, 1969. 28, 32, 35
- [51] G. Iadarola and G. Rumolo, “Electron Cloud Effects,” *ICFA Beam Dyn. Newslett.*, vol. 69, pp. 208–226, 2016. 30, 38
- [52] V. V. Anashin *et al.*, “Experimental Investigations of the Electron Cloud Key Parameters,” in *Performance improvement of electron positron collider particle factories. Proceedings, International Workshop, e+ e- Factories ’99, Tsukuba, Japan, September 21-24, 1999*, pp. 94–100, 1999. 31
- [53] R. E. Kirby and F. King, “Secondary electron emission yields from pep-ii accelerator materials,” *Nuclear Instruments and Methods in Physics Research Section A: Accelerators, Spectrometers, Detectors and Associated Equipment*, vol. 469, no. 1, pp. 1–12, 2001. 31
- [54] H. Seiler, “Secondary electron emission in the scanning electron microscope,” *Journal of Applied Physics*, vol. 54, no. 11, pp. R1–R18, 1983. 31
- [55] V. Baglin *et al.*, “The secondary electron yield of technical materials and its variation with surface treatments,” in *Particle accelerator: Proceedings, 7th European Conference, EPAC 2000, Vienna, Austria, June 26-30, 2000. Vol. 1-3*, pp. 217–221, 2000. 31, 32
- [56] M. A. Furman and M. T. F. Pivi, “Probabilistic model for the simulation of secondary electron emission,” *Phys. Rev. ST Accel. Beams*, vol. 5, p. 124404, 2002. [Erratum: *Phys. Rev. ST Accel. Beams*16,no.6,069901(2013)]. 31, 32, 34, 44, 89
- [57] R. Cimino *et al.*, “Can low energy electrons affect high energy physics accelerators?,” *Phys. Rev. Lett.*, vol. 93, p. 014801, 2004. 31, 32, 34, 35, 90
- [58] R. Cimino, L. A. Gonzalez, R. Larciprete, A. Di Gaspare, G. Iadarola, and G. Rumolo, “Detailed investigation of the low energy secondary electron yield of technical Cu and its relevance for the LHC,” *Phys. Rev. ST Accel.*

-
- Beams*, vol. 18, no. 5, p. 051002, 2015. 31, 32, 90
- [59] J. P. Verboncoeur, “Particle simulation of plasmas: review and advances,” *Plasma Physics and Controlled Fusion*, vol. 47, no. 5A, p. A231, 2005. 31
- [60] G. Bellodi, “Code comparisons and benchmarking with different sey models in electron cloud build-up simulations,” 2005. 31
- [61] E. Benedetto *et al.*, “Review and comparison of simulation codes modeling electron-cloud build up and instabilities,” in *9th European Particle Accelerator Conference (EPAC 2004) Lucerne, Switzerland, July 5-9, 2004*, 2004. 31
- [62] G. Rumolo and F. Zimmermann, “Electron cloud simulations: build-up and related effects,” *Proceedings of the Mini-Workshop on Electron-Cloud Simulations for Proton and Positron Beams*, 2002. 31, 32
- [63] F. Zimmermann, “Electron-cloud effects in the LHC,” in *ECLLOUD’02: Mini-workshop on electron-cloud simulations for proton and positron beams, CERN, Geneva, Switzerland, 15-18 Apr 2001: Proceedings*, pp. 47–55, 2002. 32
- [64] A. Andronov, “Secondary electron emission at very low electron energy,” *St. Petersburg State Polytechnical University J. Phys. Math*, no. 1 (189), 2014. 32
- [65] A. Andronov *et al.*, “Secondary electron emission yield in the limit of low electron energy,” *arXiv preprint arXiv:1309.4658*, 2013. 32
- [66] M. Belhaj, J. Roupie, O. Jbara, J. Puech, N. Balcon, and D. Payan, “Electron emission at very low electron impact energy: experimental and monte-carlo results,” *arXiv preprint arXiv:1308.1301*, 2013. 32
- [67] I. Khan, J. Hobson, and R. Armstrong, “Reflection and diffraction of slow electrons from single crystals of tungsten,” *Physical Review*, vol. 129, no. 4, p. 1513, 1963. 32
- [68] H. Heil and J. V. Hollweg, “Electron Reflection Coefficient at Zero Energy. I. Experiments,” *Phys. Rev.*, vol. 164, pp. 881–886, Dec 1967. 32
- [69] J. De Lara *et al.*, “Multipactor prediction for on-board spacecraft rf equipment with the mest software tool,” *IEEE Transactions on Plasma Science*, vol. 34, no. 2, pp. 476–484, 2006. 32

-
- [70] P. Tolias, “Low energy electron reflection from tungsten surfaces,” *arXiv preprint arXiv:1601.02047*, 2016. 32
- [71] O. Grobner, “Beam induced multipacting,” in *Proceedings of the 1997 Particle Accelerator Conference (Cat. No. 97CH36167)*, vol. 3, pp. 3589–3591, IEEE, 1997. 35, 36, 38
- [72] J. S. Berg, “Energy gain in an electron cloud during the passage of a bunch,” Tech. Rep. CERN-LHC-Project-Note-97, CERN, 1997. 35, 36, 37, 38
- [73] O. Boine-Frankenheim, E. Gjonaj, F. Petrov, F. Yaman, T. Weiland, and G. Rumolo, “Energy loss and longitudinal wakefield of relativistic short proton bunches in electron clouds,” *Physical Review Special Topics-Accelerators and Beams*, vol. 15, no. 5, p. 054402, 2012. 35, 38, 39
- [74] U. Iriso, *Electron Clouds in the Relativistic Heavy Ion Collider*. PhD thesis, University of Barcelona, 2006. 37, 45, 46
- [75] G. Franchetti, I. Hofmann, W. Fischer, and F. Zimmermann, “Incoherent effect of space charge and electron cloud,” *Physical Review Special Topics-Accelerators and Beams*, vol. 12, p. 124401, Dec 2009. 38
- [76] F. Petrov, O. Boine-Frankenheim, and O. Haas, “Interaction of relativistic short proton bunches with space charge limited electron clouds,” *Physical Review Special Topics-Accelerators and Beams*, vol. 17, no. 12, p. 121001, 2014. 39, 44
- [77] “KEKB B factory design report,” Tech. Rep. KEK-REPORT-95-07, 1995. 39
- [78] D. Alesini *et al.*, “DAΦNE operation with electron-cloud-clearing electrodes,” *Phys. Rev. Lett.*, vol. 110, p. 124801, Mar 2013. 40
- [79] C. Y. Vallgren *et al.*, “Amorphous carbon coatings for the mitigation of electron cloud in the cern super proton synchrotron,” *Physical Review Special Topics-Accelerators and Beams*, vol. 14, no. 7, p. 071001, 2011. 40
- [80] P. C. Pinto *et al.*, “Thin film coatings for suppressing electron multipacting in particle accelerators,” in *Proceedings of 2011 Particle Accelerator Conference, New York, NY, USA*, 2011. 40
- [81] G. Stupakov and M. Pivi, “Suppression of the Effective Secondary Emission Yield for a Grooved Metal Surface,” Tech. Rep. LCC-0145, SLAC-

TN-04-045, Stanford Linear Accelerator Center, Menlo Park, CA (US), 2004. 40

- [82] R. Cimino *et al.*, “Nature of the Decrease of the Secondary-Electron Yield by Electron Bombardment and its Energy Dependence,” *Phys. Rev. Lett.*, vol. 109, p. 064801, Aug 2012. 40
- [83] A. Chance, “Analysis of electron cloud effects and mitigation options: Milestone M2.4,” Tech. Rep. CERN-ACC-2018-0041, CERN, Geneva, Oct 2018. 40, 58
- [84] U. Niedermayer, O. Boine-Frankenheim, and H. De Gerssem, “Space charge and resistive wall impedance computation in the frequency domain using the finite element method,” *Physical Review Special Topics-Accelerators and Beams*, vol. 18, no. 3, p. 032001, 2015. 41
- [85] U. Niedermayer, *Determination of Beam Coupling Impedance in the Frequency Domain*. PhD thesis, Technische Universität Darmstadt, 2016-01-19. 41
- [86] <https://github.com/openeccloud/openeccloud>. 42
- [87] D. Halliday, R. Resnick, and J. Walker, *Fundamentals of physics*. John Wiley & Sons, 2013. 43
- [88] H. de Blank, “Guiding center motion,” *Fusion science and technology*, vol. 45, no. 2T, pp. 47–54, 2004. 43
- [89] U. Iriso and S. Peggs, “Maps for electron clouds,” *Physical Review Special Topics-Accelerators and Beams*, vol. 8, no. 2, p. 024403, 2005. 45
- [90] T. Demma, S. Petracca, and A. Stabile, “A physical interpretation of the cubic map coefficients describing the electron cloud evolution,” *arXiv preprint arXiv:1011.1682*, 2010. 46
- [91] N. Mounet, *The LHC Transverse Coupled-Bunch Instability*. PhD thesis, Ecole Polytechnique, Lausanne, 2012-03-16. 49
- [92] S. Arsenyev, O. Boine-Frankenheim, and D. Schulte, “FCC-hh transverse impedance budget,” Tech. Rep. CERN-ACC-2018-152, 2018. 50
- [93] H. Koivuluoto, A. Coleman, K. Murray, M. Kearns, and P. Vuoristo, “High pressure cold sprayed (hpcs) and low pressure cold sprayed (lpcs) coatings prepared from ofhc cu feedstock: overview from powder characteristics to coating properties,” *Journal of Thermal Spray Technology*,

-
- vol. 21, no. 5, pp. 1065–1075, 2012. 52
- [94] A. Malachowska, *Analysis of the cold gas spraying process and determination of selected properties of metallic coatings on polymers*. PhD thesis, Université de Limoges, 2016. 52
- [95] T. Stoltenhoff, H. Kreye, and H. Richter, “An analysis of the cold spray process and its coatings,” *Journal of Thermal spray technology*, vol. 11, no. 4, pp. 542–550, 2002. 52
- [96] I. Bellafont *et al.*, “Design of the fcc-hh beam vacuum chamber,” (to be published). 52
- [97] V. V. Danilov, “Increasing the transverse mode coupling instability threshold by RF quadrupole,” *Physical Review Special Topics-Accelerators and Beams*, vol. 1, p. 041301, Aug 1998. 56
- [98] C. Yin Vallgren, *Low secondary electron yield carbon coatings for electron cloud mitigation in modern particle accelerators*. PhD thesis, Chalmers University of Technology, 2011. 59
- [99] P. Pinto. personal communication. 60
- [100] D. Astapovych, O. Boine-Frankenheim, V. Kornilov, U. Niedermayer, and D. Schulte, “Stability Limits with Landau Damping in the FCC-hh,” *submitted to Nuclear Instruments and Methods in Physics Research Section A*. 73